A NEW HYBRID NUMERICAL SCHEME FOR SIMULATING FAULT RUPTURES WITH NEAR FAULT BULK INHOMOGENEITIES

BY

SETARE HAJAROLASVADI

THESIS

Submitted in partial fulfillment of the requirements
for the degree of Master of Science in Civil and Environmental Engineering
in the Graduate College of the
University of Illinois at Urbana Champaign, 2016

Urbana, Illinois

Advisor:

Professor Ahmed Ettaf Elbanna

ABSTRACT

The Finite Difference (FD) and the Boundary Integral (BI) Method have been used extensively to model spontaneously propagating shear cracks in a variety of engineering and geophysical applications. While FD has a large computational cost as it requires the discretization of the whole volume of interest, it can handle a greater variety of problems in comparison with BI, including bulk nonlinearities and heterogeneities. On the other hand, the BI method eliminates the necessity of simulating the wave propagation in the whole elastic medium by leveraging space-time convolutions with the source on the fault surface. The spectral implementation of the BI in particular is faster and much more computationally efficient than other bulk methods such as FD. However, the spectral boundary integral (SBI) formulation is restricted to linear elastic bulk and planar faults. This study proposes a new method, referred to herein as the "Hybrid Method", in which the two methods are combined. Benefiting from the flexibility of FD and the efficiency of BI, this method is capable of solving a wide range of problems in a computationally efficient way.

In the Hybrid Method, nonlinearities or heterogeneities may be confined to a virtual narrow strip that includes the fault or the wave source. This strip, then, is discretized using a FD scheme in space and time while the virtual boundaries of the strip are handled using the SBI formulation that represents the two elastic half spaces outside the strip. Modeling the elastodynamic response in these two halfspaces needs to be carried out by an Independent Spectral Formulation before joining them to the strip with the appropriate boundary conditions. Dirichlet and Neumann boundary conditions are imposed on the strip and the two half-spaces, respectively, at each time step to propagate the solution forward. We illustrate the accuracy and

efficiency of the method using several examples. This approach is more computationally efficient than pure FD and expands the range of applications of SBI beyond the current state of the art.

To Father and Mother

ACKNOWLEDGEMENTS

I cannot express enough thanks to my thesis advisor, Professor Ahmed Elbanna, Department of Civil and Environmental Engineering, University of Illinois at Urbana-Champaign, for his support during my Master's studies and for being a caring mentor, who always heard my concerns with patience and never discouraged me from asking questions, even trivial ones. He taught me how to be a good listener as well as communicator and on top of all how to see the big picture and think out of the box. This project wouldn't have been completed if it wasn't for his help and guidance. My insight and understanding of "Earthquake Mechanics" have been broadened and enhanced in the last two years and I have acquired many valuable new skills under his supervision.

I also would like to thank my parents, who taught me to always value education and learning and dream big, no matter how far-fetched it might seem. They taught me how important it is to try hard for what I want and never get disappointed of the failures I might face along the way and to always believe in myself and my abilities. I have always looked up to them; they are the reason that I am who I am and I cannot thank them enough for that. I extend my gratitude to my sisters, Neda and Noushin, who, although far away, supported me during my graduate studies. I am more than blessed to have such a great family who have always given me their unconditional love and attention and have helped me achieve my goals.

I thank my Professor, Dr. Ali Akbar Golafshani, Department of Civil and Environmental Engineering, Sharif University of Technology, who, unfortunately, lost his life to cancer recently. He inspired me as an undergraduate student with his immense knowledge, his

enthusiasm in teaching and his undivided attention to the students. I thank him for the generosity with which he shared every piece of his knowledge with us.

Finally, special thanks go to my boyfriend, Kiomars, for his love and support and the confidence he had in me. I thank him for always being there for me; for supporting me emotionally and being understanding.

Table of Contents

CHAPTER 1

INTRODUCTION

Earthquake rupture is a highly nonlinear phenomenon with spatiotemporal complexity at multiple scales. The nonlinearity originates primarily from the nature of the friction operating on fault surfaces which introduces a discontinuous stick slip condition at the tips of the propagating rupture. Even in the case of continuously sliding interfaces governed by rate and state laws, the friction depends nonlinearly on the slip rate and its history, creating complex feedback between the traction boundary conditions on the fault interface and the unknown field variables.

The multiscale nature of the rupture process exists in both space and time. Space-wise, a moderate size earthquake typically propagates over tens of kilometers. However, the physical processes governing the rupture propagation operates within a narrow region at the rupture tips, called the process zone, which may not exceed few millimeters in size if realistic laboratory-based friction parameters are used. Thus, at least six orders of magnitude of spatial scales need to be resolved. Time-wise, the problem is even more challenging. An earthquake episode, where rapid slip occurs, only lasts for few to tens of seconds. The time required for the rupture tip to cross a distance equivalent to the process zone is less than millisecond. However, the time required for stress buildup and the attainment of the right condition for the initiation of the friction instability during the interseismic period may be tens to hundreds of years. In that sense, to resolve the full seismic cycle, it is necessary to devise numerical and observational protocols that are capable of resolving temporal scales over nine orders of magnitudes (milliseconds to years). This is a fundamental challenge in earthquake source physics.

Earthquakes have been recorded systematically during the last hundred years. Great progress has been made since the last half of the twentieth century with the development of the reliable strong ground motion seismometers as well as the deployment of seismic arrays across critical regions in the globe. However, a hundred years on geological time scale is just minuscule and for large earthquakes, in particular, we still lack a sufficient number of records that may enable carrying out reliable statistics for hazard calculation. An attractive route to complement observational seismology and expand on the current library of records is to perform numerical simulations for earthquake cycles and generate plausible rupture scenarios that may fill the gap in our recorded seismic history.

However, for the computational models of earthquake cycles to gain credibility, they must be informed with physics-based models of the frictional, material and geometric complexity that exist in fault zones. Furthermore, the models should be able to resolve several orders of magnitude of spatial and temporal scales as discussed above. This is one of the most enduring challenges in computational mechanics and a daunting task for most supercomputers that currently exist.

A breakthrough in approaching the spatiotemporal complexity of earthquake ruptures came with the development of a special spectral boundary integral equation framework by *Lapusta et al.,* (2000). The boundary integral formulation enabled reducing the spatial dimension of the problem by one, transforming 2D problems into 1D and 3D problems in 2D. Furthermore, Lapusta et al. (2000) devised accurate adaptive time stepping algorithms and truncation of convolution integrals that enabled the simulation of a long sequence of events combining rapid slip during earthquake ruptures and slow deformation during the interseismic periods. The

algorithm developed by Lapusta et al. (2000) built upon prior work by *Cochard and Madariaga* (1994), and *Geubelle and Rice* (1995) and added several novel features in handling the convolutions and numerical integration as discussed above. Nonetheless, the method, being a boundary integral formulation, is only limited to homogeneous linear elastic bulk as it is founded on the representation theorem and the existence of an analytical expression for the Green's function. While the method may be applied, in principle, to heterogeneous linear elastic material but the lack of a closed form representation of the Green's function makes it less computationally attractive. Furthermore, the superior performance of the spectral approach and its computational efficiency is only possible for planar interfaces. This precludes the representation of rough and nonplanar faults.

Meanwhile, numerical methods based on bulk discretization such as the finite difference and finite element have been used in simulating earthquake ruptures since mid-70s and early 80s with the pioneering works of *Boore, Larner and Aki* (1971), *Andrews* (1976), *Das and Aki* (1977), *Archuleta and Day* (1980), *Day* (1982), *Virieux and Madariaga* (1982) and others. These methods are more general than boundary integral approaches and do handle heterogeneities, nonlinearities, and fault geometry complexities. Low order formulations of these methods, however, do suffer from some numerical problems such as artificial dispersion and numerical dissipation. However, in the recent years, highly accurate formulations were introduced including the spectral finite element (Komatitsch & Tromp, 1999), the discontinuous Galerkin method (Kaser & Dumbser, 2006), and higher order finite difference schemes (Kozdon, Dunham, & Nordstrom, 2013). The main computational challenge of these methods is the need to discretize the whole bulk which increases the computational burden by at least one order of magnitude compared to the integral formulation. Furthermore, due to the impracticality of

discretizing the whole earth, the computational domain must be truncated at a sufficient distance from the fault surface in such a way that it would not affect the physical solution. This motivated the introduction of several widely-used absorbing boundary conditions such as boundary viscous damping (Lysmer and Kuhlemeyer, 1969), perfectly matching layers (Berenger, 1994), and infinite elements (Bettess, 1977). However, in all these methods artificial reflections exist to varying degrees and the absorbing surface has to be taken sufficiently far from the fault surface to ensure solution accuracy. Moreover, attempts to perform cycle simulations using these volume-based methods are rare. This is partially due to the tremendous computational cost compared and the lack of a systematic approach to handle both dynamic and quasidynamic calculations in the same framework to enable simulating both earthquake rupture events and intersesismic slow deformation.

There is, thus, a need to develop a numerical algorithm that is capable of long time simulation of earthquake cycles in a bulk that may have material heterogeneity, material nonlinearity or fault surface complexity. To that end, this work proposes a novel hybrid numerical scheme that combines the finite difference method and the spectral boundary integral equation method to enable treating fault zone nonlinearities and heterogeneities with unprecedented resolution and in a more computationally efficient way. The main idea of the method is to enclose the inhomgeneities in a virtual strip that is introduced for computational purposes only. This strip is discretized using a volume-based numerical method, chosen here to be the finite difference method just for simplicity. The top and the bottom boundaries of the virtual strip are handled using the independent spectral boundary integral formulation (Geubelle & Rice, 1995) with matching discretization. The coupling between the two methods is achieved as follows. The finite difference solution of the strip provides the traction to the spectral

boundary method at each virtual interface. The spectral scheme is then used to predict the boundary displacements. These displacements are in turn applied to the strip to advance the solution to the next time step. The algorithm is described in details in the following sections. We will show some preliminary results demonstrating the accuracy and the potential of the hybrid method for simulating several classes of elastodynamics in homogeneous and heterogeneous media.

The remainder of this thesis is organized as follows. In Chapter 2, we describe the various numerical algorithms used. Chapter 3 summarizes the results of the hybrid scheme, in comparison with a pure finite difference implementation, for a number of problems including wave propagation and rupture dynamics in homogenous and heterogeneous media with possible material nonlinearity. Chapter 4 contains further discussion of the results, conclusions and future work.

CHAPTER 2

METHODOLOGY

2.1. Theoretical formulation

We consider two sets of 2-D antiplane shear problems. In the first set, we treat a linear elastic, isotropic, infinite space with a volumetric source acting at its center (Figure 2.1.a). In the second set, the same infinite space is studied with a fault plane embedded within it across which the displacement may have discontinuity (Figure 2.1.b).

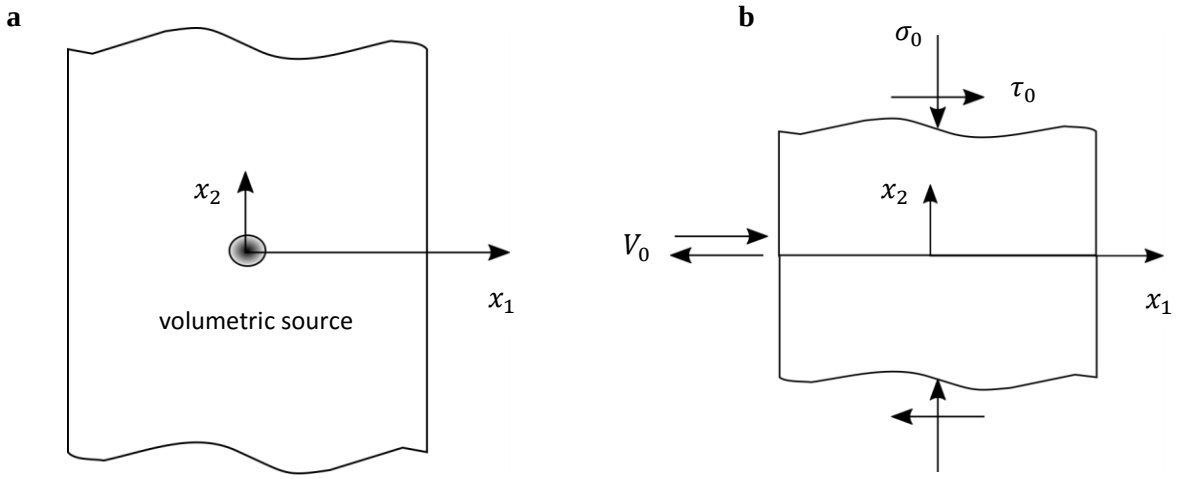

Figure 2.1- (a) Configuration of the linear-elastic, isotropic infinite space with a source at its center.(b) Configuration of the linear-elastic, isotropic infinite space with a fault surface embedded within it.

Considering a Cartesian coordinate, the equations of motion are written as

$$\rho \frac{\partial^2}{\partial t^2} u_i = \frac{\partial}{\partial x_j} \tau_{ij} + \rho\, b_i \tag{2.1}$$

Where ρ and b denote the mass and body force densities, respectively and the indices represent each component or direction in the coordinates.

The strain is defined as

$$\epsilon_{ij} = \frac{1}{2}\left(\frac{\partial u_i}{\partial x_j} + \frac{\partial u_j}{\partial x_i}\right) \tag{2.2}$$

The constitutive relation between the stress and strain is

$$\tau_{ij} = c_{ijkl}\,\epsilon_{kl} \tag{2.3}$$

and

$$c_{ijkl} = \lambda\,\delta_{ij}\,\delta_{kl} + \mu\left(\,\delta_{ik}\,\delta_{jl} + \,\delta_{il}\,\delta_{jk}\right) \tag{2.4}$$

where δ_{ij} is the Kronecker delta.

Therefore,

$$\tau_{ij} = \lambda\,\delta_{ij} u_{k,k} + \mu(u_{i,j} + u_{j,i}) \tag{2.5}$$

Substituting Equation (2.5) in (2.1) and restricting it to the 2-D antiplane problem at hand yields

$$\rho\,u_{3,tt} = \mu\,u_{3,\alpha\alpha} \qquad \alpha = 1{,}2 \tag{2.6}$$

which is the scalar wave equation.

Various numerical methods such as the Finite Difference Method (FD) and the Boundary Integral Method (BI) have been used extensively to solve problems of this kind. However, both of these methods have some limitations as explained previously. The idea is to introduce a new numerical scheme, referred to as the Hybrid Method, in which the two methods are combined in order to benefit from the flexibility of FD and the computational efficiency of BI simultaneously.

The Finite Difference and the Hybrid Method have been used to solve the abovementioned sets of problems in this work. The numerical schemes used will be explained thoroughly in the following sections.

2.2. Numerical schemes

2.2.1. Finite difference method

The finite difference scheme has been widely used since the 1970s to solve seismic wave propagation problems in elastic and inelastic media due to its simple formulation and easy implementation. Although it is the simplest scheme for modeling the seismic wave propagation and it has a high computational cost for large-scale problems, it has often proved satisfactory for exploring the earthquake dynamics and consequent ground motions (Aochi, Ulrich, Ducellier, Dupros, & Michea, 2013).

Two different finite difference schemes, each of which will be explained next, are used in this work to study the two sets of problems explained previously.

2.2.1.1. Volumetric source in a linear elastic medium

The FD scheme used in this section is explicitly explained in Appendix A.

2.2.1.2. Slip-weakening crack embedded in a linear elastic medium

A shear crack with a certain initial shear stress that is propagating spontaneously under a specified friction law is a simplified, yet useful, model of a natural earthquake. The rupture problem is highly nonlinear in its nature even when considered in its simplest form, i.e. as a discontinuity surface embedded in a linear-elastic medium. This nonlinearity is due to the fact that the problem is a mixed boundary value problem in which the time-dependent domains of displacement and traction boundary conditions depend themselves on the displacement and stress fields (Day, Dalguer, Lapusta, & Liu, 2005).

Several finite difference methods such as the Traction at Split-Node (TSN) and the inelastic-zone methods – including the Thick-Fault method (Madariaga, Olsen, & Archuleta,

1998) and the Stress-Glut method (Andrews, 1976) – have been used to solve the spontaneously-propagating shear crack problem. One of the factors influencing the accuracy of these methods is the way that the displacement discontinuity and traction is handled on the fault plane (Day et al., 2005). Here, a simpler FD method has been used which does not require using a staggered grid.

We consider a slip-weakening crack embedded in an infinite space that is isotropic and linearly elastic. The crack may be considered as a surface across which the displacement is discontinuous while the shear traction has to be continuous. The jump condition at the interface requires that 1) the shear traction be bounded by the current value of frictional strength and 2) any nonzero slip rate be opposed by an antiparallel traction (Day et al., 2005).

The frictional strength should generally evolve following a constitutive functional which may depend on the slip rate and one or more state variables. However, in this case a slip-weakening friction law, first introduced by *Ida* (1972) and *Palmer and Rice* (1973), is considered for simplicity. In the slip-weakening friction law, μ (the friction coefficient) is given by

$$\mu = \begin{cases} \mu_s - (\mu_s - \mu_d)\dfrac{\delta u}{D_c} & \delta u < D_c \\ \mu_d & otherwise \end{cases} \tag{2.7}$$

where μ_s and μ_d are coefficients of static and dynamic friction, respectively and D_c is the critical slip-weakening distance. The friction parameters are considered to be constant along the fault.

2.2.1.2.1. Formulation

Each of the domains above and below the crack is discretized with N_{ele_x} elements in the x_1 and $\frac{N_{ele_y}}{2}$ elements in the x_2 direction such that the whole domain is discretized with $N_{ele_x} \times$

N_{ele_y} elements. i and j represent node numbers in the x_1 and x_2 directions, respectively. Node-numbering in the x_2 direction for each of the lower and upper domains starts from the left-most node at the bottom at $j = 0$ and ends with $j = \frac{N_{ele_y}}{2}$. In seismology, a finite volume of the earth is usually extracted for studying. Therefore, we choose the dimensions of the strip large enough so as to avoid having any artificial reflections from the model boundaries during the simulation period (Aochi et al., 2013).

The following variables are introduced and used throughout the formulation of the problem.

$u_{i,j}^{+\,k}$: displacement value at $x_i = i\,\Delta x$ and $y_j = j\,\Delta y$ at time $t = k\Delta t$ in the upper domain

$u_{i,j}^{-\,k}$: displacement value at $x_i = i\,\Delta x$ and $y_j = j\,\Delta y$ at time $t = k\Delta t$ in the lower domain

δu_i^k: slip along the crack at $x_i = i\,\Delta x$ on the interface at time $t = k\Delta t$

Therefore,

$$\delta u_i^k = u_{i,0}^{+\,k} - u_{i,\frac{N_{ele_y}}{2}}^{-\,k} \qquad i = 0, \dots, N_{ele_x} \tag{2.8}$$

We approximate the shear stress on the crack in both domains by using a first-order finite difference estimate

$$\tau_{i,0}^{+\,k} = \tau_{i,0}^{+\,0} + \frac{\mu}{\Delta y}\left(u_{i,1}^{+\,k} - u_{i,0}^{+\,k}\right) \tag{2.9}$$

$$\tau_{i,\frac{Nele_y}{2}}^{-\,k} = \tau_{i,\frac{Nele_y}{2}}^{-\,0} + \frac{\mu}{\Delta y}\left(u_{i,\frac{Nele_y}{2}}^{-\,k} - u_{i,\frac{Nele_y}{2}-1}^{-\,k}\right) \tag{2.10}$$

To facilitate the representation of the formulae, ${\tau_{i,0}^{+}}^{k}$ and ${\tau^{-}_{i,\frac{N_{ele_y}}{2}}}^{k}$ are respectively represented by τ_i^{+k} and τ_i^{-k} from now on in the text. Similarly, ${\tau_{i,0}^{+}}^{0}$ and ${\tau^{-}_{i,\frac{Nele_y}{2}}}^{0}$ will be replaced by τ_i^{+0} and τ_i^{-0}.

Rearranging the terms, we get

$$ {u_{i,0}^{+}}^{k} = {u_{i,1}^{+}}^{k} - \left(\frac{\tau_i^{+k} - \tau_i^{+0}}{\mu}\right)\Delta y \tag{2.11} $$

$$ {u^{-}_{i,\frac{N_{ele_y}}{2}}}^{k} = {u^{-}_{i,\frac{N_{ele_y}}{2}-1}}^{k} + \left(\frac{\tau_i^{-k} - \tau_i^{-0}}{\mu}\right)\Delta y \tag{2.12} $$

By the continuity of shear along the interface,

$$ \tau_i^{+k} = \tau_i^{-k} = \tau_i^k \tag{2.13} $$

Therefore, subtracting equations (2.11) and (2.12) yields

$$ \delta u_i^k = \left({u_{i,1}^{+}}^{k} - {u^{-}_{i,\frac{N_{ele_y}}{2}-1}}^{k}\right) + 2\Delta y\left(\frac{\tau_i^0 - \tau_i^k}{\mu}\right) \tag{2.14} $$

In a slip-weakening friction law, μ (the friction coefficient) is given by (2.7) where μ_s and μ_d are the coefficients of static and dynamic friction, respectively and D_c is the critical slip-weakening distance. Assuming that the friction coefficients do not vary along the fault, we can, then, write the frictional shear strength as

$$ \tau^f = \begin{cases} \left(\mu_s - (\mu_s - \mu_d)\dfrac{\delta u}{D_c}\right)\sigma & \delta u < D_c \\ \mu_d\,\sigma & otherwise \end{cases} \tag{2.15} $$

Therefore, in discretized form we have

$$\tau_i^f = \begin{cases} \left(\mu_s - (\mu_s - \mu_d)\frac{\delta u_i}{D_c}\right)\sigma_i & \delta u_i < D_c \\ \mu_d\ \sigma_i & otherwise \end{cases} \tag{2.16}$$

In the beginning, each arbitrary node i along the crack will be at rest unless τ_i^0 exceeds the static frictional strength $\mu_s\sigma_i$. As time goes by, the crack starts propagating and determining the regions at which it will evolve or become arrested will depend on the history of slip and tractions at that node.

At the nodes that slip is accumulating, the frictional shear strength should be equal to the shear stress on the interface and at the nodes that the crack is locked (no slip accumulation), the shear stress varies with time and can be different than the frictional strength but does not exceed the static friction (the first requirement of the jump condition). When the shear stress value does reach the static friction, the node will be on the verge of moving and slip starts to accumulate.

Having this mechanism in mind, an updating scheme is presented in the following section.

2.2.1.2.2. Updating scheme

Assuming that all field variables are known for all nodes in the upper and lower domains at time *t*,

1. Set $t = t + \Delta t$
2. Update the value of displacement for all internal nodes (all nodes except those on the edges of the two domains). For a more detailed explanation, see the derivation of Equation (A.8) in Appendix A.

$$u_{i,j}^{+\,k+1} = 2\,u_{i,j}^{+\,k} - u_{i,j}^{+\,k-1} + r^2\left(u_{i+1,j}^{+\,k} + u_{i-1,j}^{+\,k} + u_{i,j+1}^{+\,k} + u_{i,j-1}^{+\,k} - 4\,u_{i,j}^{+\,k}\right) \tag{2.17a}$$

$$u_{i,j}^{-\,k+1} = 2\,u_{i,j}^{-\,k} - u_{i,j}^{-\,k-1} + r^2\left(u_{i+1,j}^{-\,k} + u_{i-1,j}^{-\,k} + u_{i,j+1}^{-\,k} + u_{i,j-1}^{-\,k} - 4\,u_{i,j}^{-\,k}\right) \tag{2.17b}$$

In the above formulae, i ranges from 1 to $N_{ele_x} - 1$ and j ranges from 1 to $\frac{N_{ele_y}}{2} - 1$.

3. Impose zero boundary conditions to all edge nodes except the ones on the frictional interface. Notice that assuming fixed edges will not have an effect on our simulation, because we choose the dimensions of the strip big enough to avoid reflections during the simulation period.

$$u_{i,\frac{N_{ele_y}}{2}}^{+\,k+1} = 0 \qquad i = 0, \dots, N_{ele_x}$$

$$u_{0,j}^{+\,k+1} = u_{N_{ele_x},j}^{+\,k+1} = 0 \qquad j = 0, \dots, \frac{N_{ele_y}}{2} \tag{2.18a}$$

$$u_{i,0}^{-\,k+1} = 0 \qquad i = 0, \dots, N_{ele_x}$$

$$u_{0,j}^{-\,k+1} = u_{N_{ele_x},j}^{-\,k+1} = 0 \qquad j = 0, \dots, \frac{N_{ele_y}}{2} \tag{2.18b}$$

Next, in order to update the value of displacement at the nodes on the frictional interface, we follow step 4 for all nodes along the crack.

4. Determine V_i^k the slip rate at each node using a backward difference scheme

$$V_i^k = \frac{\delta u_i^k - \delta u_i^{k-1}}{\Delta t} \tag{2.19}$$

Assuming V_i to be constant and equal to V_i^k in $[t, t+\Delta t]$, if $V_i^k \leq 0$, the crack is locked at this point; therefore, no additional slip accumulates and we will have

$$\delta u_i^{k+1} = \delta u_i^k \tag{2.20}$$

- Using Equation (2.14), calculate the shear stress on the interface in terms of slip at time $t + \Delta t$

$$\tau_i^{k+1} = \tau_i^0 + \frac{\mu}{2\Delta y}\left(u_{i,1}^{+\,k+1} - u^{-}_{i,\frac{Nele_y}{2}-1}{}^{k+1} - \delta u_i^{k+1}\right) \tag{2.21}$$

- Compare the shear stress value with the static frictional strength.

If $\tau_i^{k+1} < \mu_s \sigma_i$, the point remains at rest and the calculation for slip (Equation 2.20) is valid.

If $\tau_i^{k+1} \geq \mu_s \sigma_i$, the point is on the verge of sliding and therefore the calculation for slip and shear stress (Equations 2.20 and 2.21) are not valid. In this case, we have to set the shear stress equal to the frictional shear strength. The value of the frictional strength, however, is determined by the value of slip itself and depending on whether slip is greater or less than the critical slip-weakening distance, different expressions should be used for determining the frictional strength. Since we do not have the slip value yet, we assume that the accumulated slip is less than D_c. This assumption will be checked later on.

$$\tau_i^{k+1} = \tau_i^f \tag{2.22}$$

Therefore,

$$\tau_i^0 + \frac{\mu}{2\Delta y}\left(u_{i,1}^{+\,k+1} - u^{-}_{i,\frac{Nele_y}{2}-1}{}^{k+1} - \delta u_i^{k+1}\right) = \left(\mu_s - (\mu_s - \mu_d)\frac{\delta u_i^{k+1}}{D_c}\right)\sigma_i \tag{2.23}$$

Rearranging the terms, we get

$$\delta u_i^{k+1} = \frac{\left({u_{i,1}^+}^{k+1} - {u^-_{i,\frac{Nele_y}{2}-1}}^{k+1} \right) + \frac{2\Delta y}{\mu}(\tau_i^0 - \mu_s \sigma_i)}{1 - \frac{2\,\Delta y}{D_c}\,\frac{\sigma_i(\,\mu_s - \mu_d\,)}{\mu}} \tag{2.24}$$

Checking the assumption: if $\delta u_i^{k+1} \geq D_c$, set

$$\tau_i^0 + \frac{\mu}{2\Delta y}\left({u_{i,1}^+}^{k+1} - {u^-_{i,\frac{Nele_y}{2}-1}}^{k+1} - \delta u_i^{k+1} \right) = \mu_d \sigma_i \tag{2.25}$$

Rearranging the terms, we get

$$\delta u_i^{k+1} = \left({u_{i,1}^+}^{k+1} - {u^-_{i,\frac{Nele_y}{2}-1}}^{k+1} \right) + \frac{2\Delta y}{\mu}(\tau_i^0 - \mu_d \sigma_i) \tag{2.26}$$

- If $V_i^k > 0$, the point is sliding; therefore, the value of slip can be calculated by going through Equations (2.23) to (2.26).

5. Update the displacement values on the frictional interface using Equations (2.11) and (2.12).

$${u_{i,0}^+}^{k+1} = {u_{i,1}^+}^{k+1} - \left(\frac{{\tau_i^+}^{k+1} - {\tau_i^+}^0}{\mu} \right) \Delta y \tag{2.27}$$

$${u^-_{i,\frac{Nele_y}{2}}}^{k+1} = {u^-_{i,\frac{Nele_y}{2}-1}}^{k+1} + \left(\frac{{\tau_i^-}^{k+1} - {\tau_i^-}^0}{\mu} \right) \Delta y \tag{2.28}$$

2.2.2. Hybrid method

Although the finite difference method can handle a great variety of problems, including bulk nonlinearities and heterogeneities, that cannot otherwise be treated with boundary integral methods, and proves to be satisfactory for modeling unsolved physical problems due to its simple formulation and easy implementation (Aochi et al., 2013), it has a large computational cost as it requires the discretization of the whole volume of interest. Whereas the boundary integral methods, which have been widely used to study spontaneous propagation of cracks in elastic media, are faster and much more computationally efficient since they eliminate the necessity of simulating the wave propagation in the whole elastic medium by leveraging space-time convolutions with the source on the fault surface (Day et al., 2005). Therefore, the Hybrid Method, which is the combination of both and benefits from the flexibility of FD and the computational efficiency of BI, can be exploited to study a wider spectrum of problems that are difficult to explore otherwise.

In the Hybrid Method, nonlinearities or heterogeneities may be confined to a virtual narrow strip that includes the fault or the wave source. This strip, then, is discretized using a FD scheme in space and time while the virtual boundaries of the strip are handled using the SBI formulation that represents the two elastic half spaces outside the strip. Modeling the elastodynamic response in these two halfspaces needs to be carried out by an Independent Spectral Formulation before joining them to the strip with the appropriate boundary conditions (Breitenfeld & Geubelle, 1998). Dirichlet and Neumann boundary conditions are imposed on the strip and the two half-spaces, respectively, at each time step to propagate the solution forward.

As it was mentioned above, one of the core concepts in this method is the use of the Independent Spectral Formulation as was introduced by *Geubelle and Rice* (1995). We use a

velocity formulation and implement convolution integral truncation and time step updates as discussed in *Lapusta et al.* (2000). The derivation of the method is included in Appendix B for completeness. Interested readers may also refer to *Geubelle and Rice* (1995) and *Breitenfeld and Geubelle* (1998) for more extended discussions.

2.2.2.1. Updating scheme

In this formulation, the Boundary Integral Equation Method (BIEM) is used to model the response of the two half-spaces and the Finite Difference Method (FD) is used to model the response of the virtual strip.

The general configuration of the model is shown in Figure 2.2. It is assumed that the strip has a width equal to "*a"* and a thickness equal to *"b"* with *a* much greater than *b*. There are N_{ele_x} elements in the *x* direction and N_{ele_y} elements in the *y* direction. Square-shaped elements are considered in the strip to keep the error in the FD scheme uniform. The element size is dictated by the properties of the BIEM model.

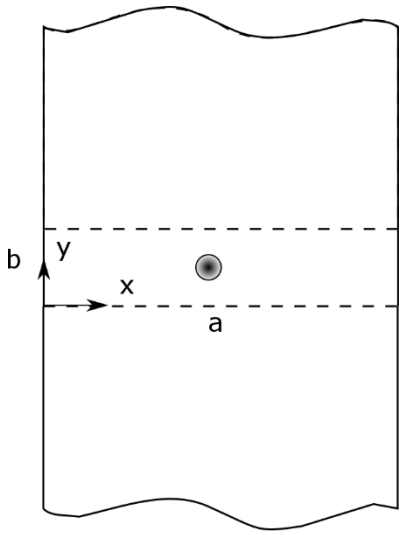

Figure 2.2- General configuration of the problem for the coupled formulation with a volumetric source at the center of the strip.

Consider the initial distribution of displacement at $t = 0$. This distribution will cause some initial shear stress on the interfaces of the strip and the two halfspaces. We know that

$$\tau_{yz} = \mu \frac{\partial u_z}{\partial y} \tag{2.29}$$

Therefore, using a one-sided second-order finite difference, we have, in discrete form

$$\tau^0_{i,0} = \mu \frac{-u^0_{i,2} + 4u^0_{i,1} - 3u^0_{i,0}}{\Delta y} \qquad i = 0, \dots, N_{ele_x} \tag{2.30a}$$

$$\tau^0_{i,N_{ele_y}} = \mu \frac{3u^0_{i,N_{ele_y}} - 4u^0_{i,\,N_{ele_y}-1} + u^0_{i,\,N_{ele_y}-2}}{\Delta y} \qquad i = 0, \dots, N_{ele_x} \tag{2.30b}$$

These values are imposed as the initial tractions on the edges of the two half-spaces.

Note that the nodes defined for the BIEM formulation are actually not at the same location as the nodes defined in the FD algorithm (Figure 2.3). In the BIEM formulation, calculations are based on the values of the field variables at the cell centers whereas in the FD formulation, the nodes are located at the cell corners.

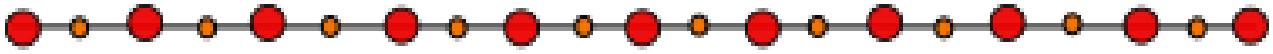

Figure 2.3- Configuration of the edge nodes for the FD and BIEM algorithms. The red and orange nodes show the FD and BIEM nodes respectively.

Therefore, in order to determine the initial tractions, interpolation is required

$$\tau^+_i = \frac{1}{2}\left(\tau^0_{i-1,N_{ele_y}} + \tau^0_{i,N_{ele_y}}\right) \qquad i = 1, \dots, N_{ele_x} \tag{2.31a}$$

$$\tau^-_i = \frac{1}{2}\left(\tau^0_{i-1,0} + \tau^0_{i,0}\right) \qquad i = 1, \dots, N_{ele_x} \tag{2.31b}$$

τ_i^+ is the traction at the cell center of the i[th] cell on the upper half plane and τ_i^- is the traction at the cell center of the i[th] cell on the lower half plane. Since we have the values of the displacements at $t = 0$ based on the Gaussian source (or whatever other initial distribution of displacement that's being used), calculation of the stress functionals f^+, f^- and therefore the values of the initial shear stress on the two interfaces τ^+, τ^- will be possible with the following formulae

$$\tau^+(x,t) = \tau_0^+(x) + f^+(x,t) - \frac{\mu}{c_s} V^+(x,t) \tag{2.32a}$$

$$\tau^-(x,t) = \tau_0^-(x) + f^-(x,t) + \frac{\mu}{c_s} V^-(x,t) \tag{2.32b}$$

In discrete form we have

$$\tau_i^+(t) = \tau_i^{0^+} + f_i^+(t) - \frac{\mu}{c_s} V_i^+(t) \tag{2.33a}$$

$$\tau_i^-(t) = \tau_i^{0^-} + f_i^-(t) + \frac{\mu}{c_s} V_i^-(t) \tag{2.33b}$$

Assume that the values of displacement are known at time *t*.

1. In the Finite Difference algorithm, calculate the values of shear stress on the edge nodes using the following formulae

$$\tau_{i,N_{ele_y}}^k = \mu \frac{3u_{i,N_{ele_y}}^k - 4u_{i,N_{ele_y}-1}^k + u_{i,N_{ele_y}-2}^k}{\Delta y} \qquad i = 0, \dots, N_{ele_x} \tag{2.34a}$$

$$\tau_{i,0}^k = \mu \frac{-u_{i,2}^k + 4u_{i,1}^k - 3u_{i,0}^k}{\Delta y} \qquad i = 0, \dots, N_{ele_x} \tag{2.34b}$$

2. Interpolate and make the required adjustments to determine the tractions on the edges of the two half-planes.

$$\tau_i^+(t) = \frac{-1}{2}\left(\tau^k_{i-1,N_{ele_y}} + \tau^k_{i,N_{ele_y}}\right) \qquad i = 1, \dots, N_{ele_x} \tag{2.35a}$$

$$\tau_i^-(t) = \frac{1}{2}\left(\tau^k_{i-1,0} + \tau^k_{i,0}\right) \qquad i = 1, \dots, N_{ele_x} \tag{2.35b}$$

3. Determine the values of velocities at time *t* using the following formulae.

$$\tau_i^+(t) = \tau_{0_i}^+ + f_i^+(t) - \frac{\mu}{c_s} V_i^+(t) \qquad i = 1, \dots, N_{ele_x} \tag{2.36a}$$

$$\tau_i^-(t) = \tau_{0_i}^- + f_i^-(t) + \frac{\mu}{c_s} V_i^-(t) \qquad i = 1, \dots, N_{ele_x} \tag{2.36b}$$

4. Make first predictions for the values of displacement at time $t + \Delta t$, based on known values at time t, as

$$u_i^{+^*}(t + \Delta t) = u_i^+(t) + V_i^+(t)\,\Delta t \qquad i = 1, \dots, N_{ele_x} \tag{2.37a}$$

$$u_i^{-^*}(t + \Delta t) = u_i^-(t) + V_i^-(t)\,\Delta t \qquad i = 1, \dots, N_{ele_x} \tag{2.37b}$$

5. Make a corresponding first prediction $f_i^{+^*}(t + \Delta t)$ and $f_i^{-^*}(t + \Delta t)$ of the functionals, using displacement predictions from the previous step and treating the slip rates as if they were constant through the time step Δt and equal to $V_i(t)$. To implement this in the spectral formulation, we first compute the Fourier coefficients of $V_i^+(t)$, $V_i^-(t)$ and $u_i^{+^*}(t + \Delta t)$ and $u_i^{-^*}(t + \Delta t)$. To represent FFT operations, we use the following relations.

For the upper half plane, we have

$$\dot{D}_n^+(t) = \sum_{i=1}^{N_{ele_x}} V_i^+(t)\, W_N^{(i-1)(n-1)} \tag{2.38a}$$

$$D_n^{+^*}(t+\Delta t) = D_n^+(t) + \Delta t\, \dot{D}_n^+(t) \tag{2.39a}$$

$$\begin{aligned} F_n^{+^*}(t+\Delta t) = -\mu|k_n| \Bigg[& D_n^{+^*}(t+\Delta t) \\ & - \int_{\Delta t}^{t+\Delta t} W(|k_n| c_s t') \dot{D}_n^+(t+\Delta t - t') dt' \\ & - \dot{D}_n^+(t) \int_0^{\Delta t} W(|k_n| c_s t') dt' \Bigg] \end{aligned} \tag{2.40a}$$

$$f_i^{+^*}(t+\Delta t) = \frac{1}{N_{ele_x}} \sum_{n=1}^{N_{ele_x}} F_n^{+^*}(t+\Delta t)\, W_N^{-(i-1)(n-1)} \tag{2.41a}$$

For the lower halfplane, we have

$$\dot{D}_n^-(t) = \sum_{i=1}^{N_{ele_x}} V_i^-(t)\, W_N^{(i-1)(n-1)} \tag{2.38b}$$

$$D_n^{-^*}(t+\Delta t) = D_n^-(t) + \Delta t\, \dot{D}_n^-(t) \tag{2.39b}$$

$$F_n^{-*}(t+\Delta t) = \mu|k_n|\Bigg[D_n^{-*}(t+\Delta t) - \int_{\Delta t}^{t+\Delta t} W(|k_n|c_s t')\dot{D}_n^{-}(t+\Delta t-t')dt' - \dot{D}_n^{-}(t)\int_0^{\Delta t} W(|k_n|c_s t')dt'\Bigg] \tag{2.40b}$$

$$f_i^{-*}(t+\Delta t) = \frac{1}{N_{ele_x}}\sum_{n=1}^{N_{ele_x}} F_n^{-*}(t+\Delta t)\, W_N^{-(i-1)(n-1)} \tag{2.41b}$$

Here, $W_N = e^{\frac{(-2\pi i)}{N_{ele_x}}}$ where $i = \sqrt{-1}$ and W is the convolution kernel for the velocity formulation in the 2-D antiplane case (Lapusta, Rice, Ben-Zion, & Gutuan, 2000).

6. Use the displacement values obtained in step 4 to calculate the displacement values at the FD nodes. [1]

$$u_{i,N_{ele_y}}^{k+1} = \frac{1}{2}\left(u_i^{+*}(t+\Delta t) + {u_{i+1}^{+}}^{*}(t+\Delta t)\right) \qquad i = 1, \dots, N_{ele_x} - 1 \tag{2.42a}$$

$$u_{i,0}^{k+1} = \frac{1}{2}\left(u_i^{-*}(t+\Delta t) + {u_{i+1}^{-}}^{*}(t+\Delta t)\right) \qquad i = 1, \dots, N_{ele_x} - 1 \tag{2.42b}$$

7. Use the displacement values calculated in the previous step and repeat steps 1 to 3 to predict an estimate for $V_i^{+*}(t+\Delta t)$, $V_i^{-*}(t+\Delta t)$.

8. Calculate the final prediction of displacement at time $t+\Delta t$ by

[1] It should be noted that the value of the displacement at the first and last FD nodes cannot be found by interpolation with the BIEM field values since the number of BIEM nodes (cell centers) is less than that of the FD. This, however, is not a problem because the displacement values at these nodes are already set to zero as part of the boundary conditions for the FD.

$$u_i^{+**}(t+\Delta t) = u_i^{+}(t) + \frac{\Delta t}{2}\left[V_i^{+}(t) + V_i^{+*}(t+\Delta t)\right] \qquad i = 1, \dots, N_{ele_x} \tag{2.43a}$$

$$u_i^{-**}(t+\Delta t) = u_i^{-}(t) + \frac{\Delta t}{2}\left[V_i^{-}(t) + V_i^{-*}(t+\Delta t)\right] \qquad i = 1, \dots, N_{ele_x} \tag{2.43b}$$

9. Make a corresponding prediction $f_i^{+**}(t+\Delta t)$ and $f_i^{-**}(t+\Delta t)$ of the functional, using the $u_i^{+**}(t+\Delta t)$ and $u_i^{-**}(t+\Delta t)$ and assuming velocities as if they were constant and equal to $\frac{1}{2}\left[V_i^{+}(t) + V_i^{+*}(t+\Delta t)\right]$ and $\frac{1}{2}\left[V_i^{-}(t) + V_i^{-*}(t+\Delta t)\right]$ throughout the time step. This is consistent with updating the slip in step 8. Updating the functionals is similar to what was done in step 5.
10. Use the corrected displacement values obtained in step 8 to calculate the displacement values at the FD nodes and get a more accurate estimate of $\tau^{+}(t+\Delta t)$ and $\tau^{-}(t+\Delta t)$ on the boundary.
11. Make final predictions $V_i^{+**}(t+\Delta t)$, $V_i^{-**}(t+\Delta t)$ of the velocities, similar to step 7.
12. Set the values of the field quantities $u_i^{+}(t+\Delta t)$, $u_i^{-}(t+\Delta t)$, $V_i^{+}(t+\Delta t)$, $V_i^{-}(t+\Delta t)$ equal to the predictions with the superscript double asterisks.

The updating scheme proposed above can also be used for the case of a slip-weakening crack embedded in a linear elastic bulk with some modifications in handling the shear stress on the boundaries and updating the FD scheme in each time step.

CHAPTER 3

RESULTS

In this chapter, the results of five problems that have been solved with both methods are presented to show that the finite difference and the hybrid method yield similar results. Each problem statement is fully explained and the accuracy of the hybrid method against a sole Finite Difference algorithm is tested.

3.1. Volumetric source in a linear elastic homogeneous bulk

Consider two linear elastic, homogeneous halfspaces with a shear modulus of $\mu = 30000\ MPa$ and a width of $a = 8\ km$ (Figure 3.1).

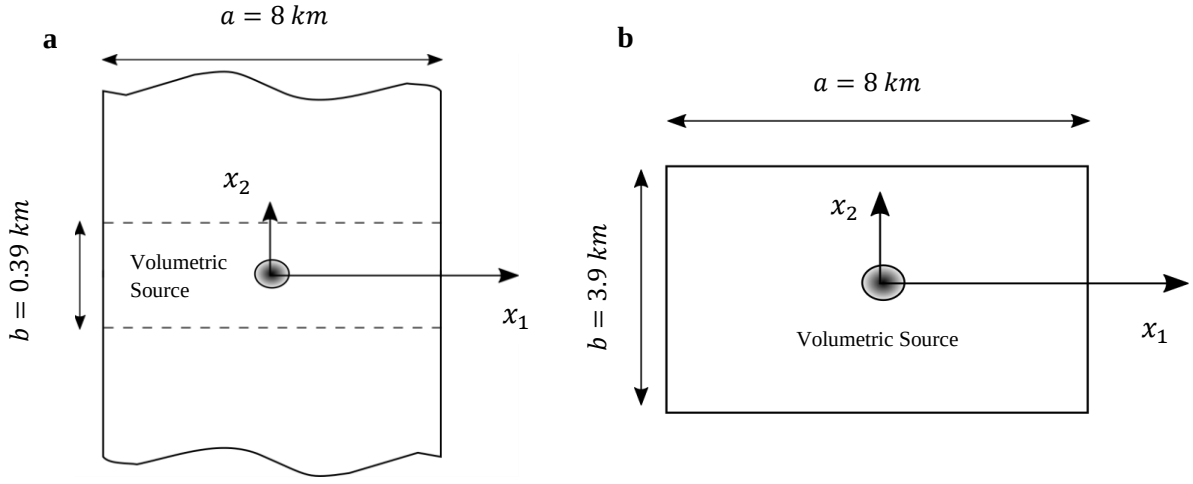

Figure 3.1- (a) Configuration of the problem in the Hybrid method. (b) Configuration of the problem in the FD method.

We choose a virtual strip of thickness 0.39 km in between. Notice that the thickness of the strip "*b"* is chosen to be way smaller than its width "*a"* which means that the waves arrive at the interfaces with the halfspaces way sooner than they reach the other two boundaries of the strip. Therefore, we do not have to worry about reflections that will appear once the waves hit the boundaries of the strip in the x_2 direction with zero displacement boundary conditions.

In the FD method, we attempt to solve the following boundary value problem on the strip.

$$\begin{cases} u_{tt} = c_s^2 \left(u_{xx} + u_{yy}\right) \\ u(0,y,t) = u(a,0,t) = 0 \\ u(x,0,t) = u(x,b,t) = 0 \\ u(x,y,0) = f(x,y) \\ u_t(x,y,0) = 0 \end{cases} \tag{3.1}$$

where $c_s = \sqrt{\frac{\mu}{\rho}}$ is the shear wave speed and $f(x,y)$ represents the volumetric source.

In the hybrid method, the same formulation is considered except that the boundary conditions on the interfaces are dictated by the elastodynamic response of the halfspaces calculated through BIEM.

3.1.1. Gaussian source

In this case, f in Equation (3.1) is a 2-D Gaussian source.

$$f(x,y) = A \exp\left(-\left(\frac{(x-x_0)^2}{2\,\sigma_x^2} + \frac{(y-y_0)^2}{2\,\sigma_y^2}\right)\right) \tag{3.2}$$

Where A is the amplitude, (x_0, y_0) is the center, and σ_x, σ_y are the x and y spreads of the blob. We have chosen$A = 1, \sigma_x = 0.1$ and $\sigma_y = 0.05$. (x_0, y_0) will always be the center of the strip depending on the strip dimensions and the origin of the Cartesian coordinates (Figure 3.2).

Square elements are used in the Finite Difference model to keep the error uniform. The size of the elements is dictated by the properties of the BIEM model. The shear wave speed is assumed to be 3 km/s and CFL conditions are imposed. If adoptive time stepping is used (see *Lapusta et al.* 2000), we have to make sure that the time step is identical in both models in order to have a fair comparison of the results.

Three sets of meshes ($N_{ele_x} = 1024, N_{ele_x} = 2048$ and $N_{ele_x} = 4096$) are used to discretize the strip and study the effects of refinement on the results in both methods and assess convergence. An error analysis is also carried out to study the effect of mesh refinement on the absolute error.

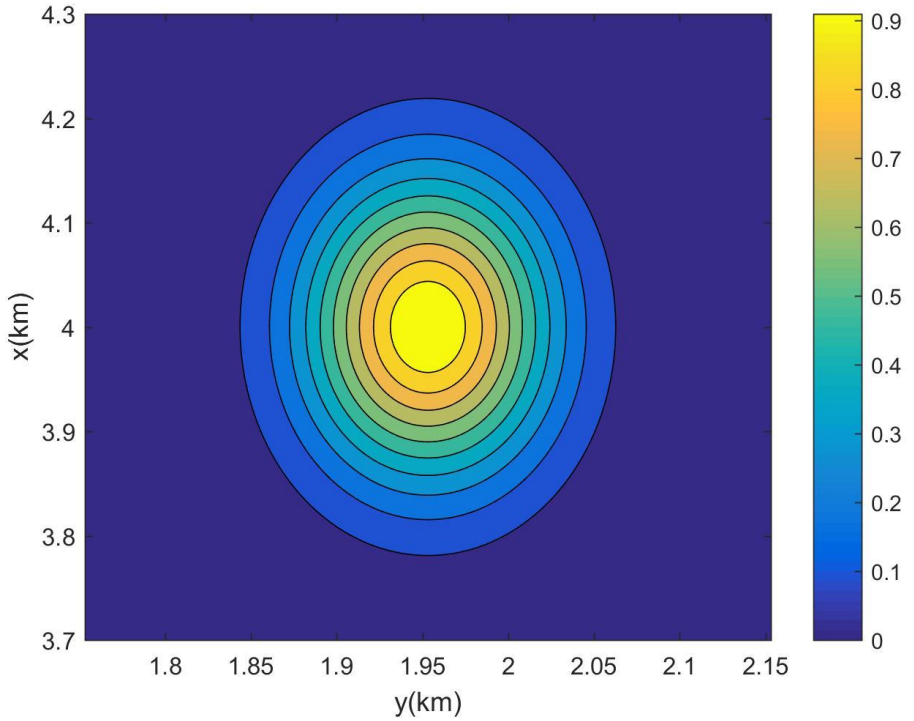

Figure 3.2- Contour for the Gaussian source.

Figure 3.3 shows the time history of a point right at the middle of the strip and a point at the center of the boundary for the finest mesh. As expected, the displacement time history for the point at the center of the strip starts at 1 (m) which is the peak value used for the Gaussian source and diminishes to zero as the waves get further away. The displacement time history for the point at the middle of the virtual boundary, though, starts at zero – since the waves have not reached the boundary yet–, reaches its peak at some point and again decreases to zero as the waves move

away from the boundary. It can be seen that the time history of these points are identical in both methods meaning that the coupled formulation is able to predict the response quite accurately.

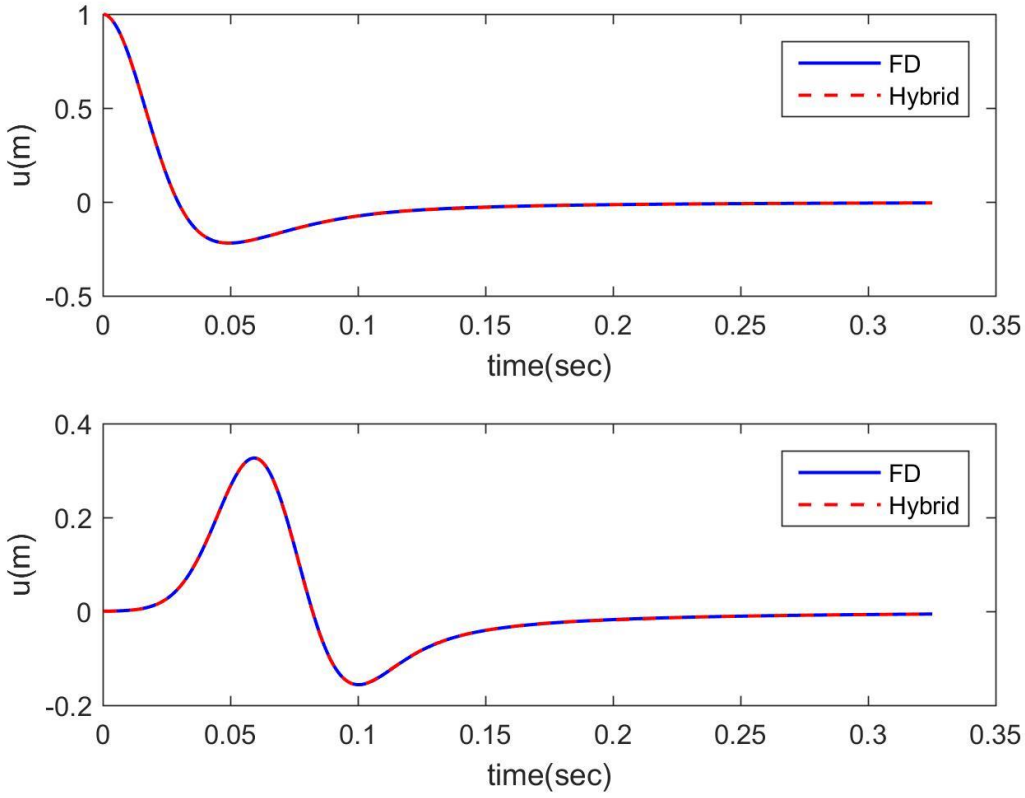

Figure 3.3- Time history plots. Top: Time history of a point at the middle of the strip. Bottom: Time history of a point at the center of the boundary.

Next, we will also look at the spatial distribution of the displacement fields for the finest mesh as a complement to the time history plots. In Figure 3.4, the displacement profiles along a line parallel to the x_1 axis at the center of the virtual strip are compared every 100 time steps. Figure 3.5 shows a similar comparison of displacement values along a line parallel to the x_1 axis on the boundary of the virtual strip. It is evident from the figures that the results are identical.

Figure 3.6 compares the absolute errors in the three different meshes used. The absolute error is defined as the difference between the displacement values obtained from the two methods. It can be seen that the error decreases with mesh refinement which guarantees convergence.

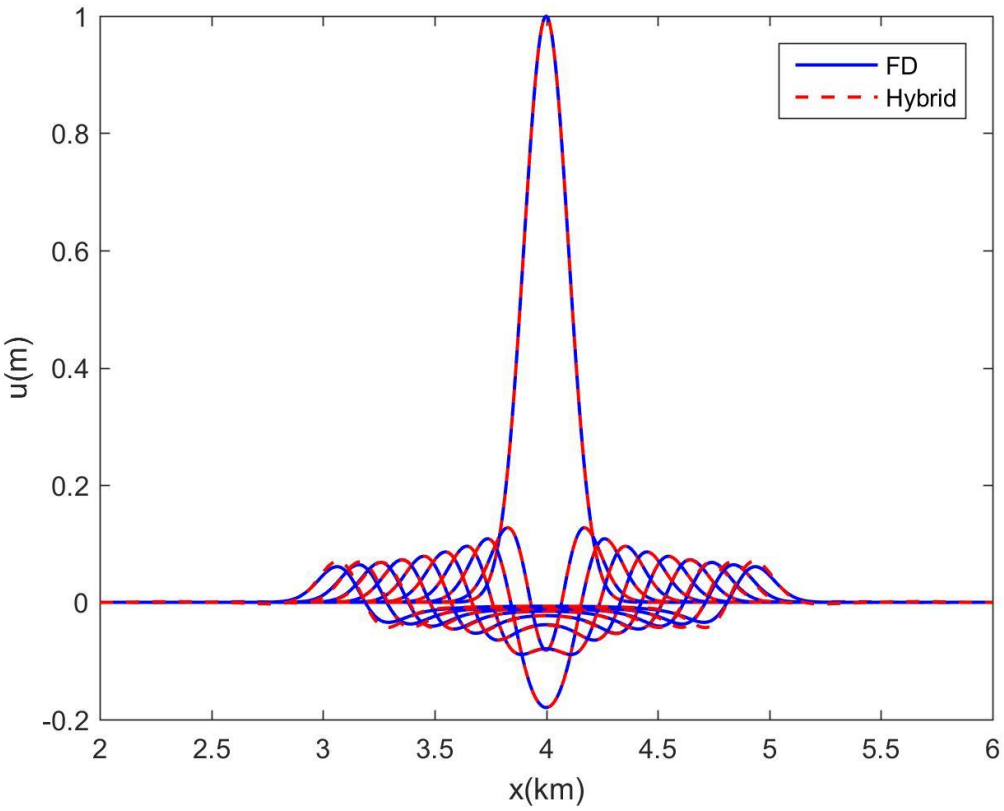

Figure 3.4- Comparison of the displacement profile along a line parallel to the x_1 axis and at the middle of the strip for the two methods. The displacement plots are provided every 100 time steps with time increasing as the maximum peak values decrease.

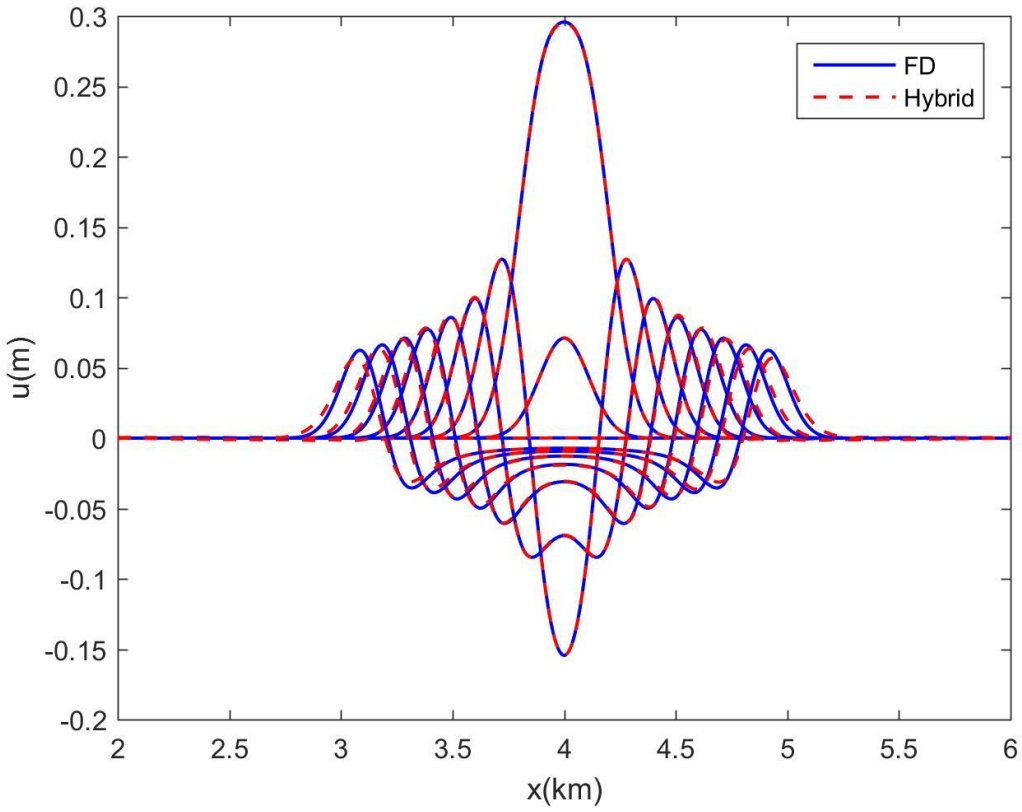

Figure 3.5- Comparison of the displacement profile along a line parallel to the x_1 axis and at the boundary of the strip for the two methods. The displacement plots are provided every 100 time steps with time increasing as the peaks move from the center to the sides.

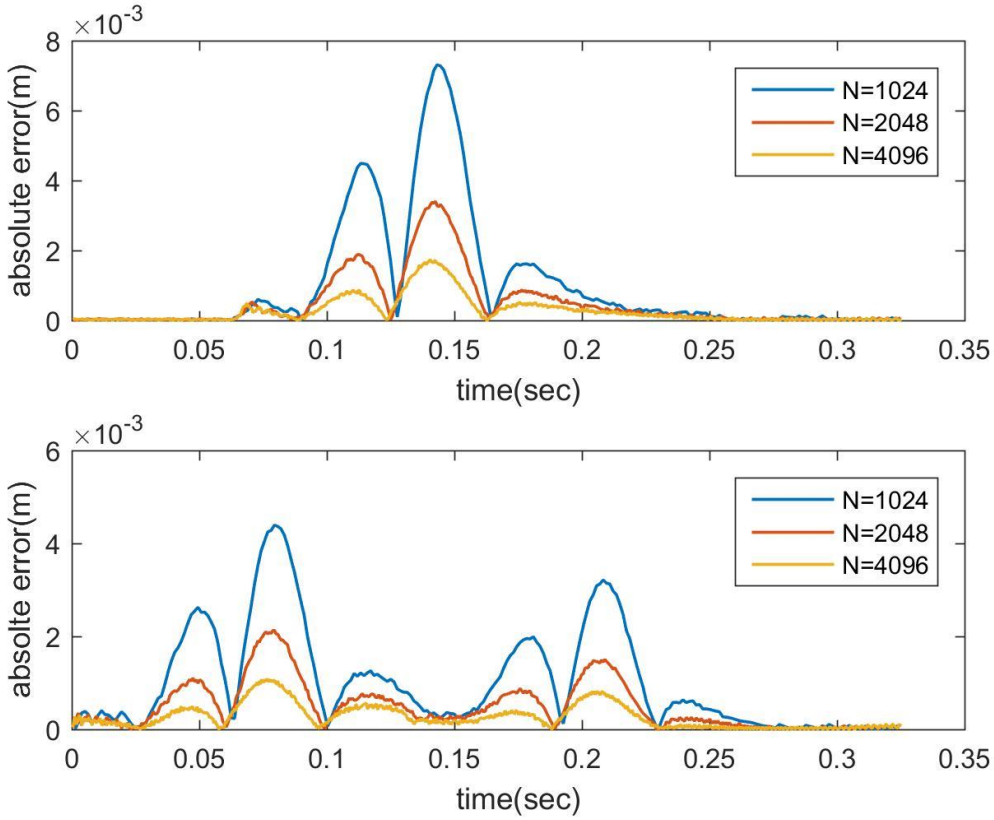

Figure 3.6- Error analysis plots. Top: error values for a point at the center of the strip. Bottom: error values for a point at the middle of the boundary.

3.1.2. Square source

Next, we consider the same problem as in section 3.1.1 but now with a square source as shown in Figure 3.7. The initial displacement is 0.1 (m) in the square region shown below and zero everywhere else.

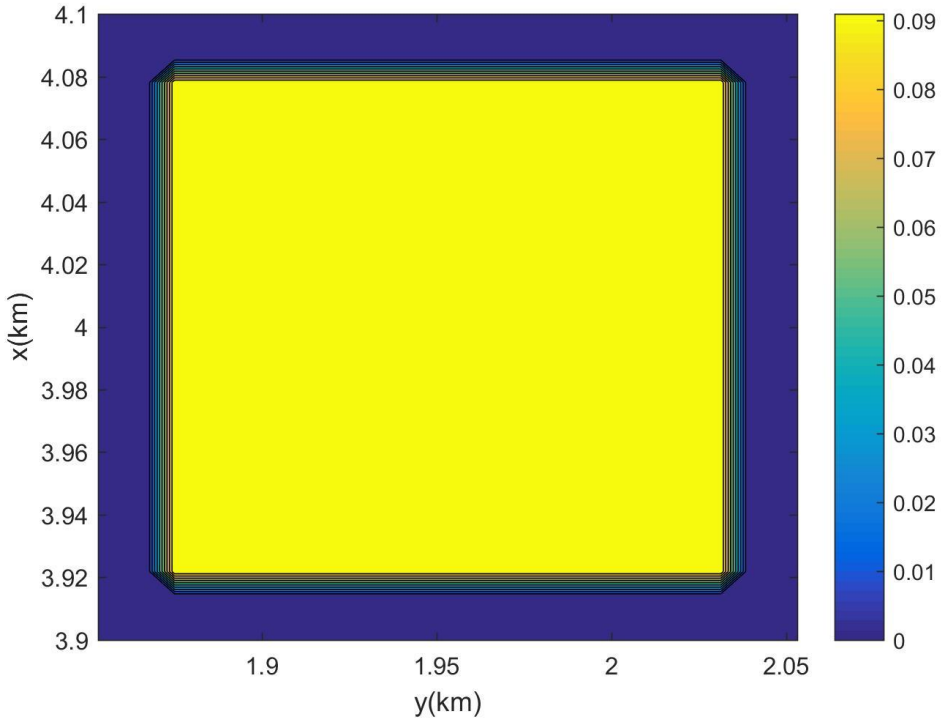

Figure 3.7- Contour for the Square source.

The model properties are the same as what was explained in the previous example. Three meshes are used as before and an error analysis is carried out at the end.

The results for the finest mesh are shown in Figures 3.8 through 3.10. The plots for displacement along lines parallel to the x_1 axis are made every 200 time steps and are shown in different subplots since the oscillations in the solutions can make it difficult to discern the solutions at different times. It can be seen from the figures that the Hybrid method gives a slightly smoother solution than the FD in this case.

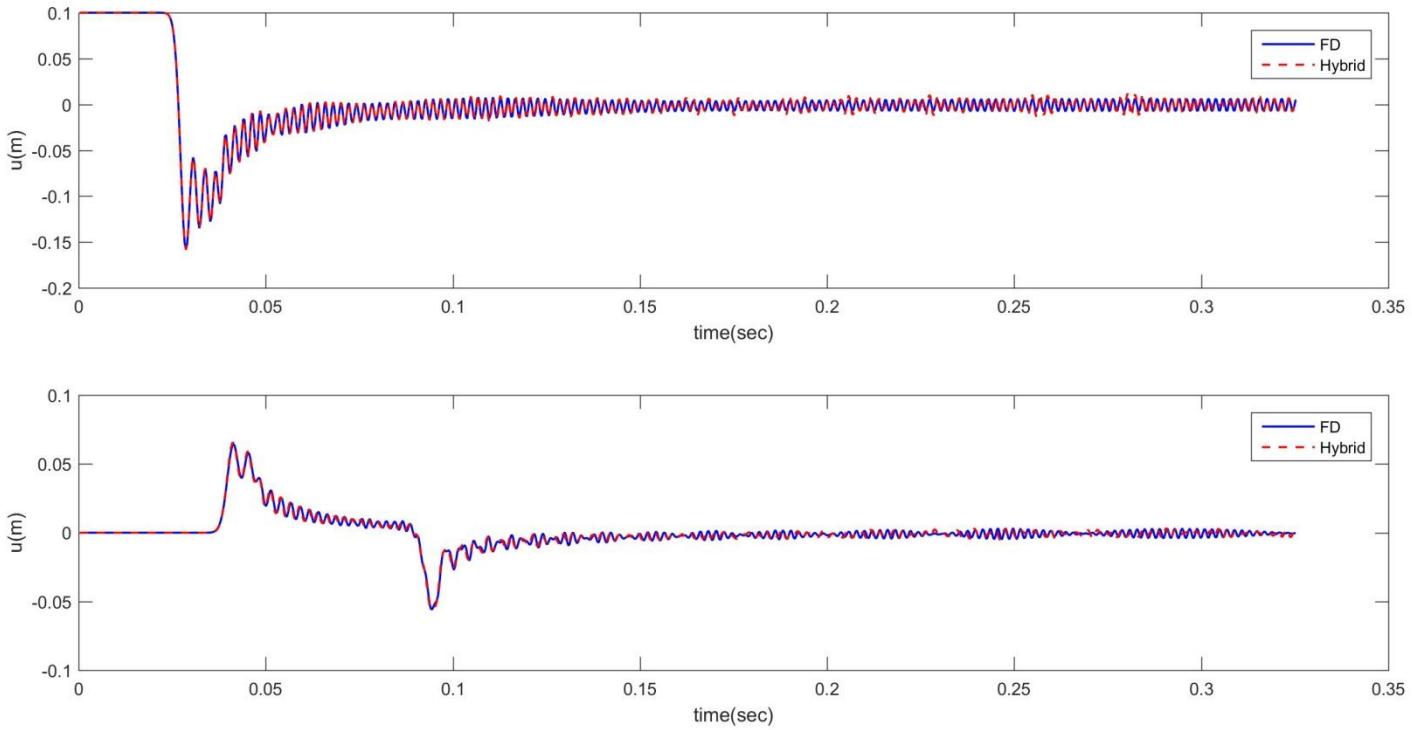

Figure 3.8- Time history plots. Top: Time history of a point at the middle of the strip. Bottom: Time history of a point at the center of the boundary.

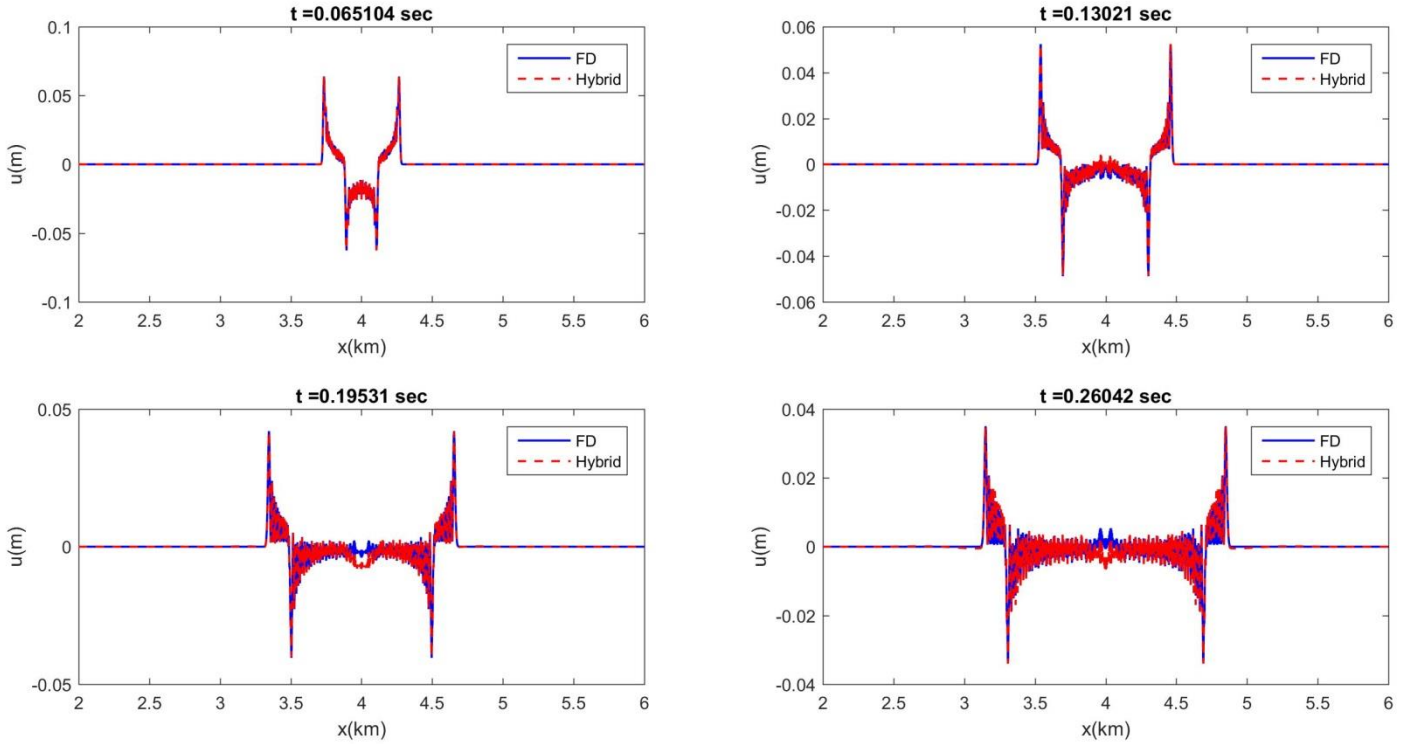

Figure 3.9- Comparison of the displacement profile along a line parallel to the x_1 axis and at the middle of the strip for the two methods. The displacement plots are provided every 200 time steps.

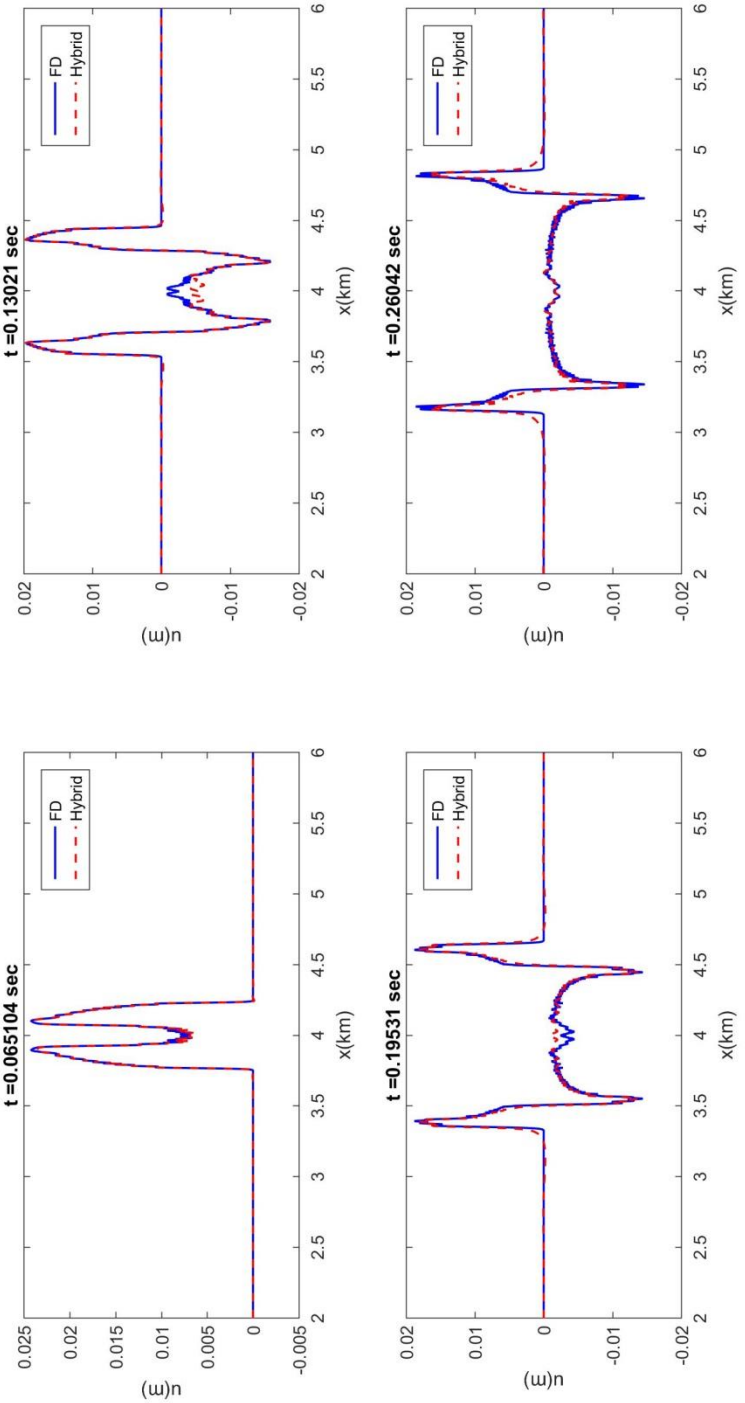

Figure 3.10- Comparison of the displacement profile along a line parallel to the x_1 axis and at the boundary of the strip for the two methods. The displacement plots are provided every 200 time steps.

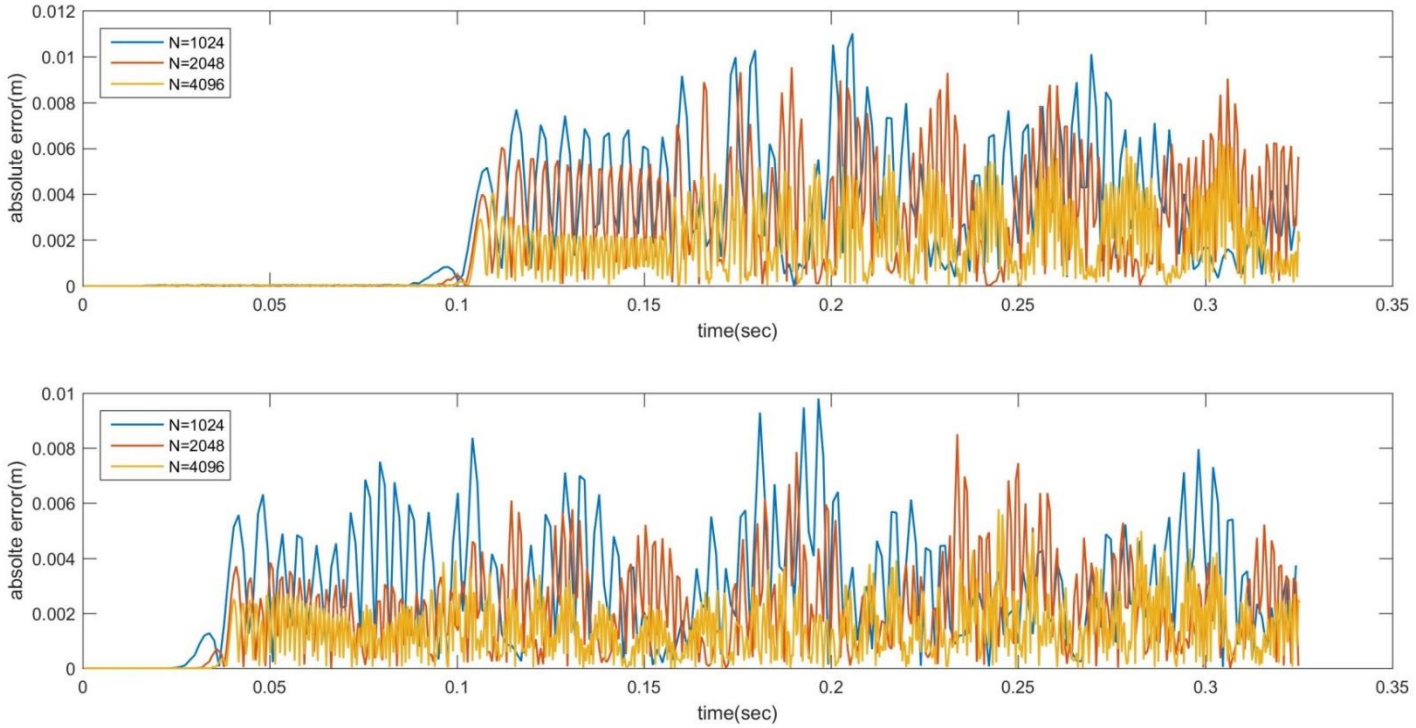

Figure 3.11- Error analysis plots. Top: error values for a point at the center of the strip. Bottom: error values for a point at the middle of the boundary.

The figures show that even in the case of a discontinuous wave source, the two methods agree to a very good extent and the levels of error are low. Also, the Hybrid method can be a better choice in such cases since the finite difference method generally shows a more oscillatory behavior with discontinuous sources. Figure 3.11 also shows that the error decreases with mesh refinement which guarantees convergence.

3.2. Antiplane shear crack with constant friction

Consider an 8 km crack with a specified initial normal stress distribution (Figure 3.13) embedded in a homogeneous, linearly elastic medium with a shear modulus of 30000 MPa and a density of 2670 kg/m^3. A high normal stress is considered outside the mid-region. This serves as a barrier and prevents the crack from expanding beyond the middle region, which has a relatively lower normal stress (100 MPa). The configuration of the problem for both methods is shown in the figure below.

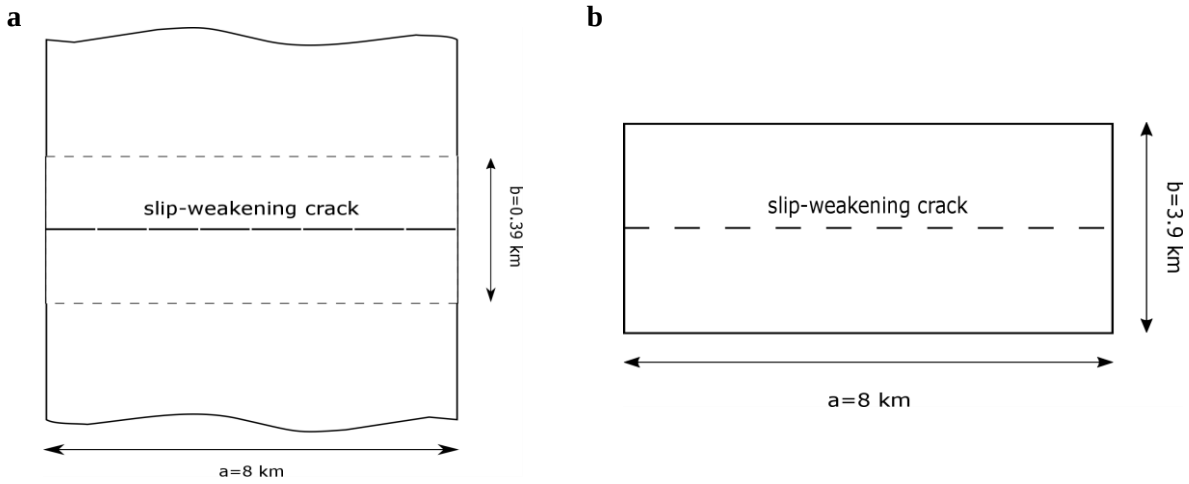

Figure 3.12- (a) Configuration of the problem in the Hybrid method. (b) Configuration of the problem in the FD method.

A constant friction coefficient $\mu_s = \mu_d = 0.6$ is assumed along the crack. The critical slip-weakening distance D_c is set equal to 0.4 meters. The problem is solved once with the Finite

Difference Method and another time with the coupled formulation. The results are presented in the figures that follow for the finest mesh.

Square elements are used in the Finite Difference model to keep the error uniform with the size of the elements dictated by the properties of the BIEM model. CFL condition is imposed.

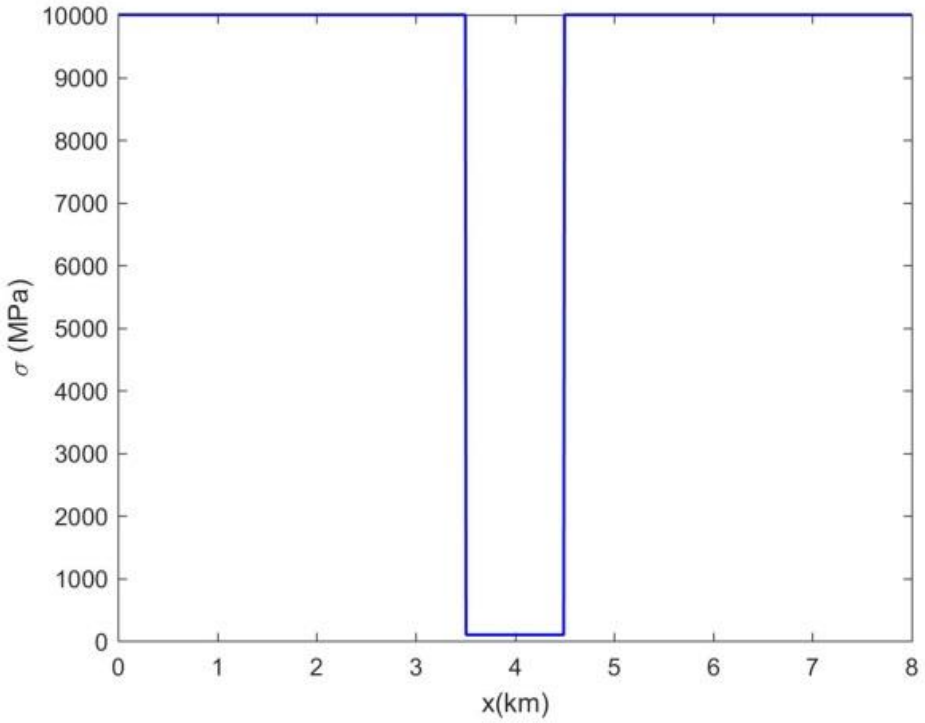

Figure 3.13- normal stress distribution for an antiplane shear crack with constant friction.

Three sets of meshes ($N_{ele_x} = 1024, N_{ele_x} = 2048$ and $N_{ele_x} = 4096$) are used to discretize the strip and study the effects of refinement on the results in both methods and assess convergence. An error analysis is also carried out to study the effect of mesh refinement on the absolute error.

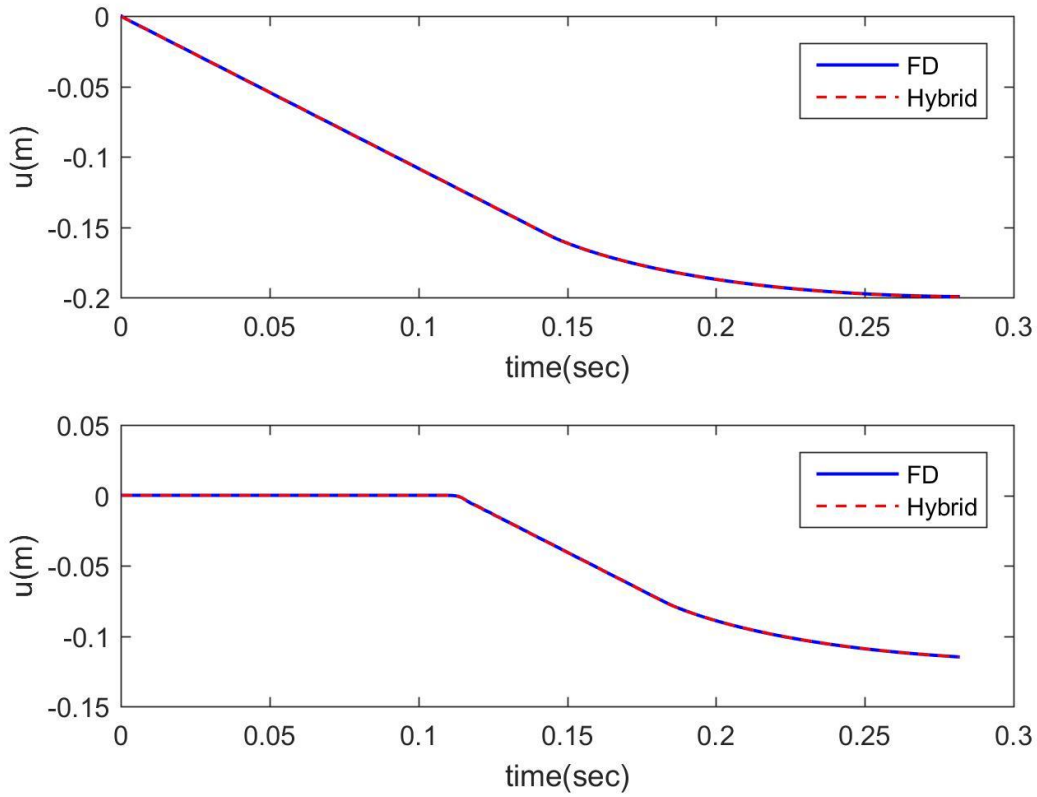

Figure 3.14- Time history plots. Top: Time history of a point at the middle of the crack on the lower halfplane. Bottom: Time history of a point at the center of the lower boundary of the strip.

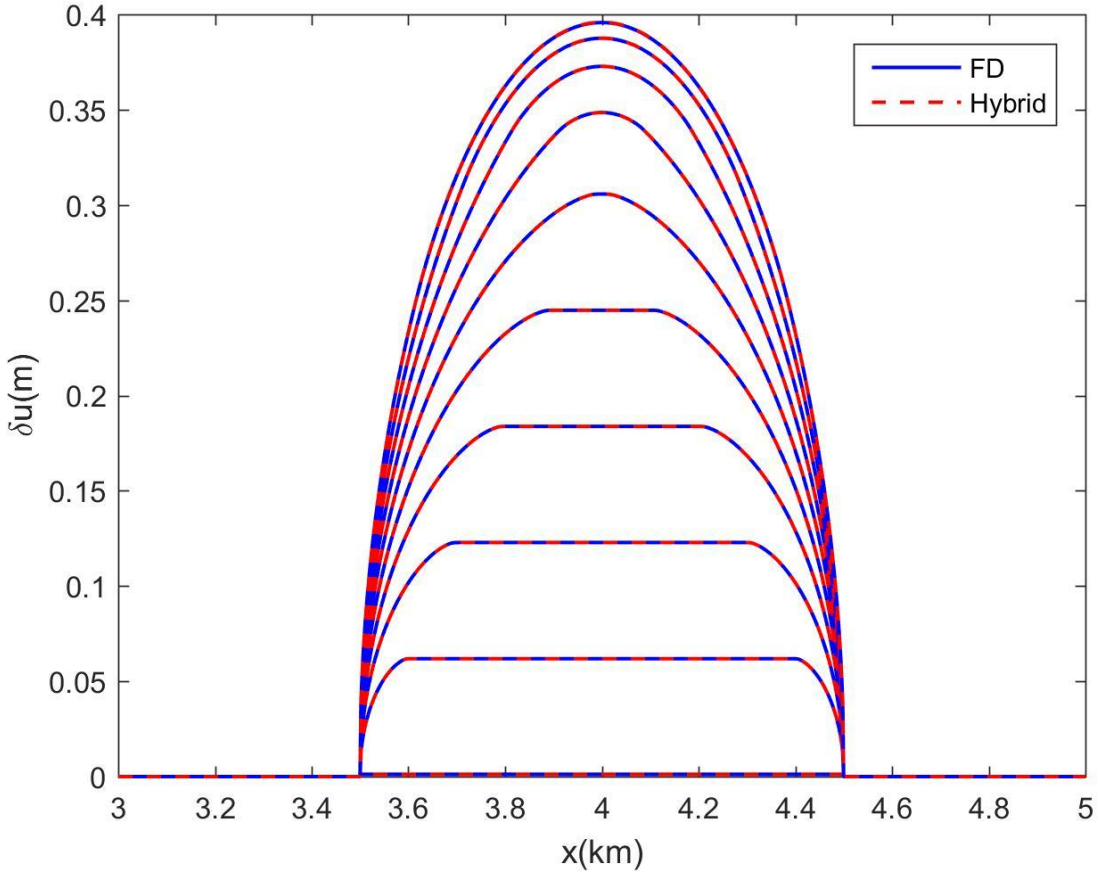

Figure 3.15- Comparison of the slip profiles along the crack for the two methods. The plots are provided every 100 time steps with time increasing as the maximum peak values increase.

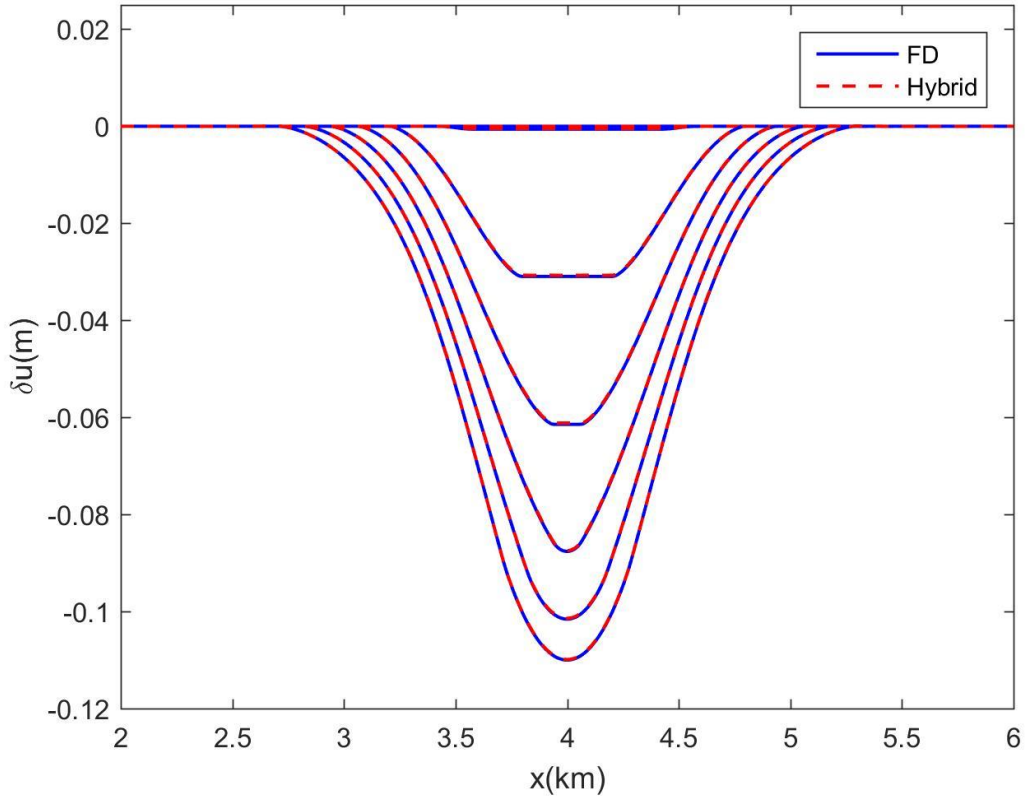

Figure 3.16- Comparison of the displacement profiles along a line parallel to the x_1 axis and on the lower boundary of the strip for the two methods. The displacement plots are provided every 100 time steps with time increasing as the absolute peak values increase.

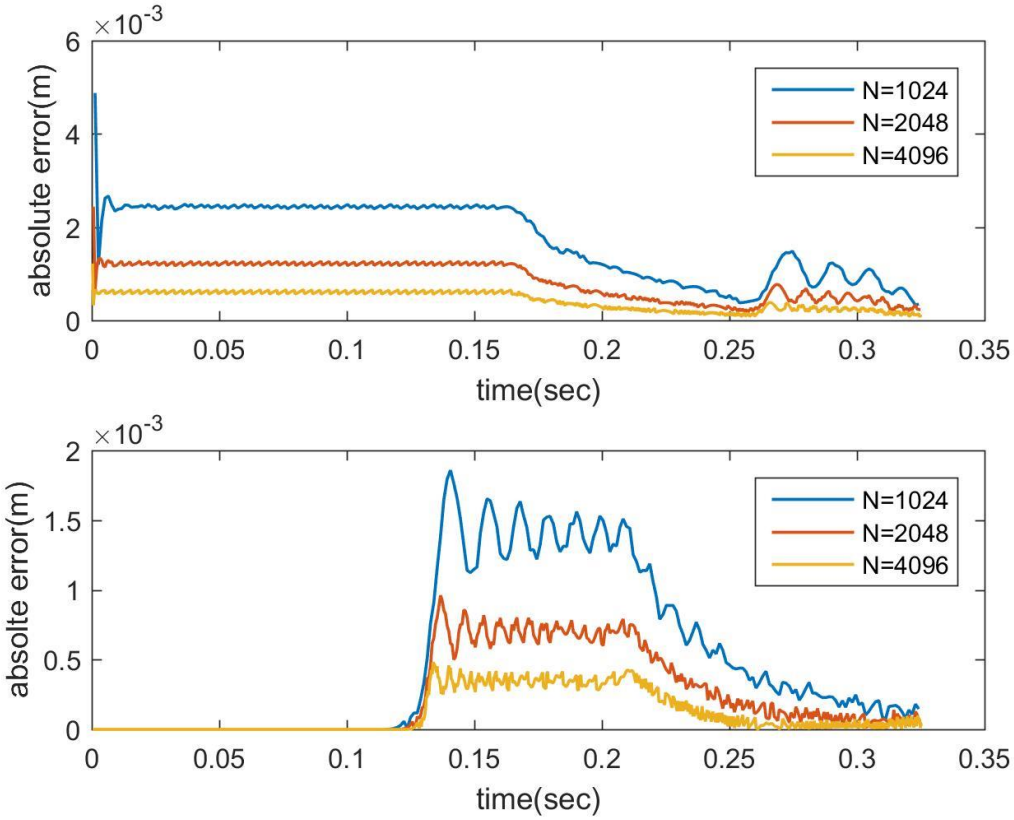

Figure 3.17- Error analysis plots. Top: absolute error of the slip values for a point at the center of the crack. Bottom: absolute error of the displacement values for a point at the middle of the boundary.

3.3. Antiplane shear crack with a slip-weakening friction law

In this section, a more complicated version of the previous problem is studied to verify our results. While the configuration of the problem is as shown in Figure 3.12, the normal stress outside the mid-region is reduced to 120 MPa to allow the crack to expand. Also, a slip-weakening friction law is used, which is more realistic than the assumption of a constant friction along the crack. In the slip-weakening friction law, μ (the friction coefficient) is given by

$$\mu = \begin{cases} \mu_s - (\mu_s - \mu_d)\dfrac{\delta u}{D_c} & \delta u < D_c \\ \mu_d & otherwise \end{cases} \tag{3.3}$$

where μ_s and μ_d are coefficients of static and dynamic friction, respectively and D_c is the critical slip-weakening distance. Here, $\mu_s = 0.6$, $\mu_d = 0.33$ and $D_c = 0.4\ (m)$. Other model properties are the same as the previous example. Three sets of meshes are used as before to study the problem. The results for the finest mesh are presented in the figures that follow.

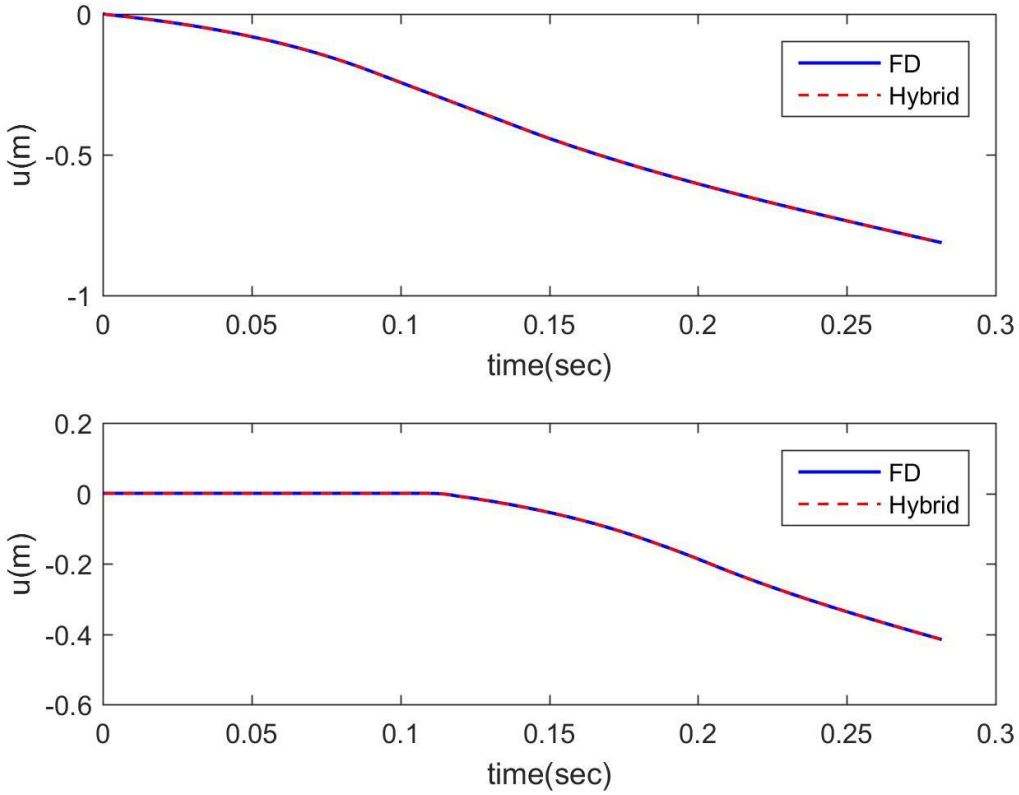

Figure 3.18- Time history plots. Top: Time history of a point at the middle of the crack on the lower halfplane. Bottom: Time history of a point at the center of the lower boundary of the strip.

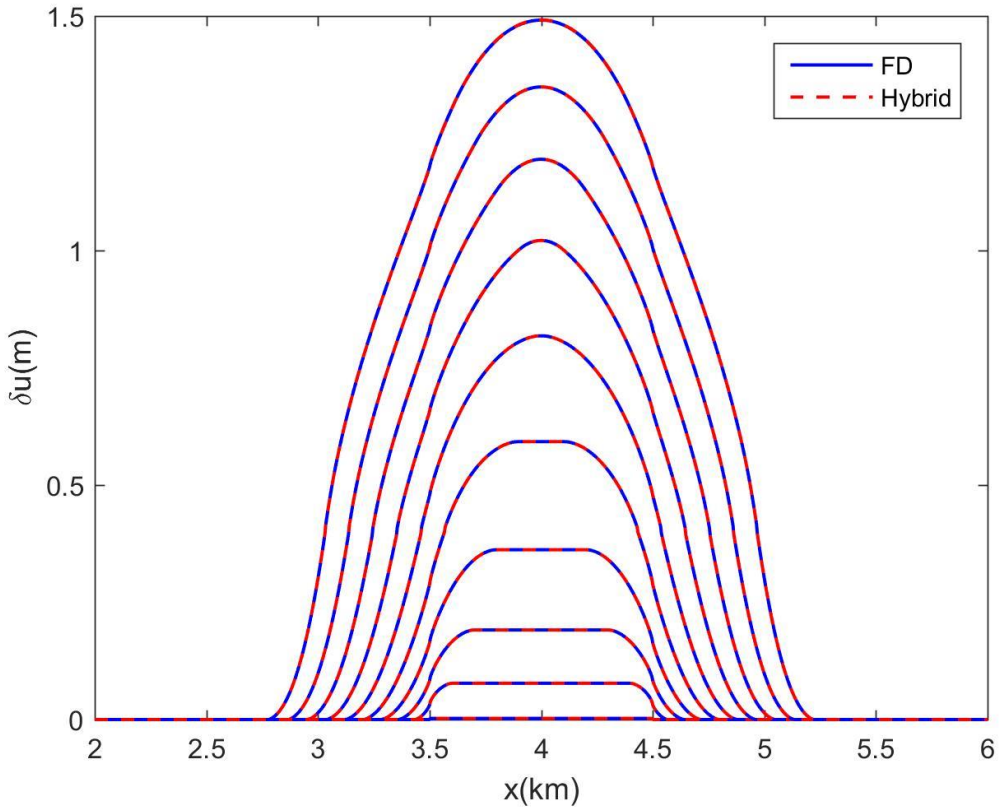

Figure 3.19- Comparison of the slip profiles along the crack for the two methods. The plots are provided every 100 time steps with time increasing as the maximum peak values increase.

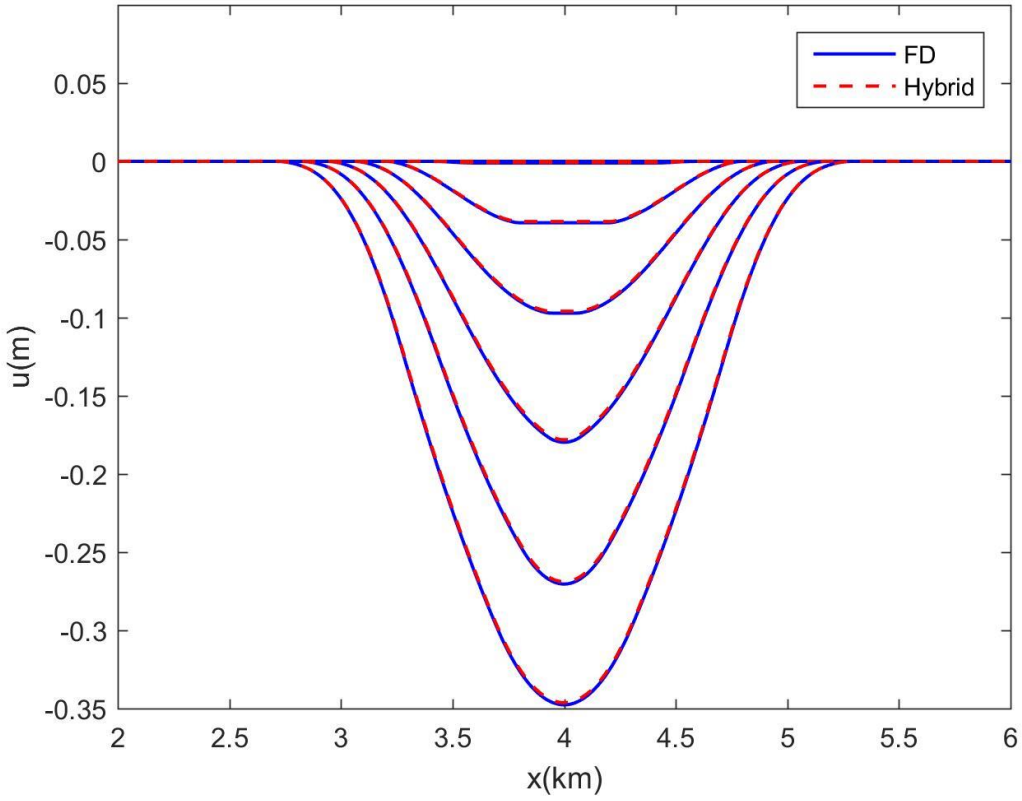

Figure 3.20- Comparison of the displacement profiles along a line parallel to the x_1 axis and on the lower boundary of the strip for the two methods. The displacement plots are provided every 100 time steps with time increasing as the absolute peak values increase.

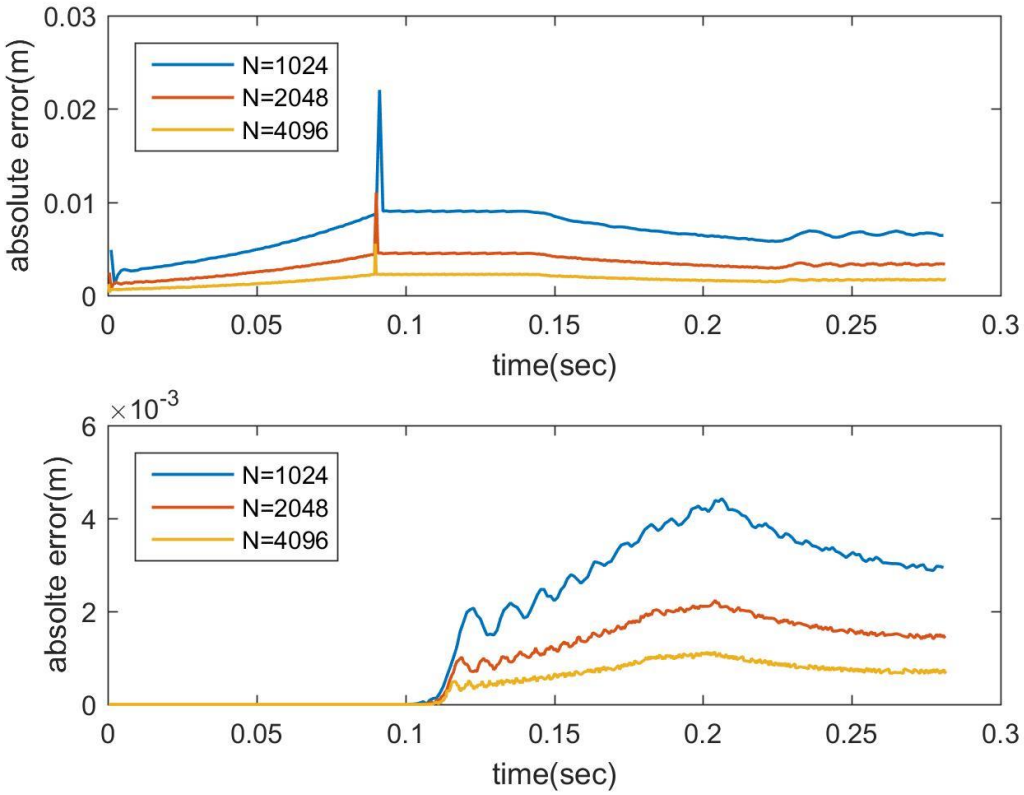

Figure 3.21- Error analysis plots. Top: absolute error of the slip values for a point at the center of the crack. Bottom: absolute error of the displacement values for a point at the middle of the boundary.

3.4. Linear elastic heterogeneous material with a Gaussian source

A strip of 8 km width with a Gaussian source at its center is considered. The mid-region of the strip is assumed to have a shear modulus of 30000 MPa while the two remaining regions have a shear modulus of 33000 MPa and are attached to two half-spaces with the same shear modulus. The softer material has been placed closer to the crack since this is normally the case in real faults. The geometry of the strip is shown in Figure 3.22.

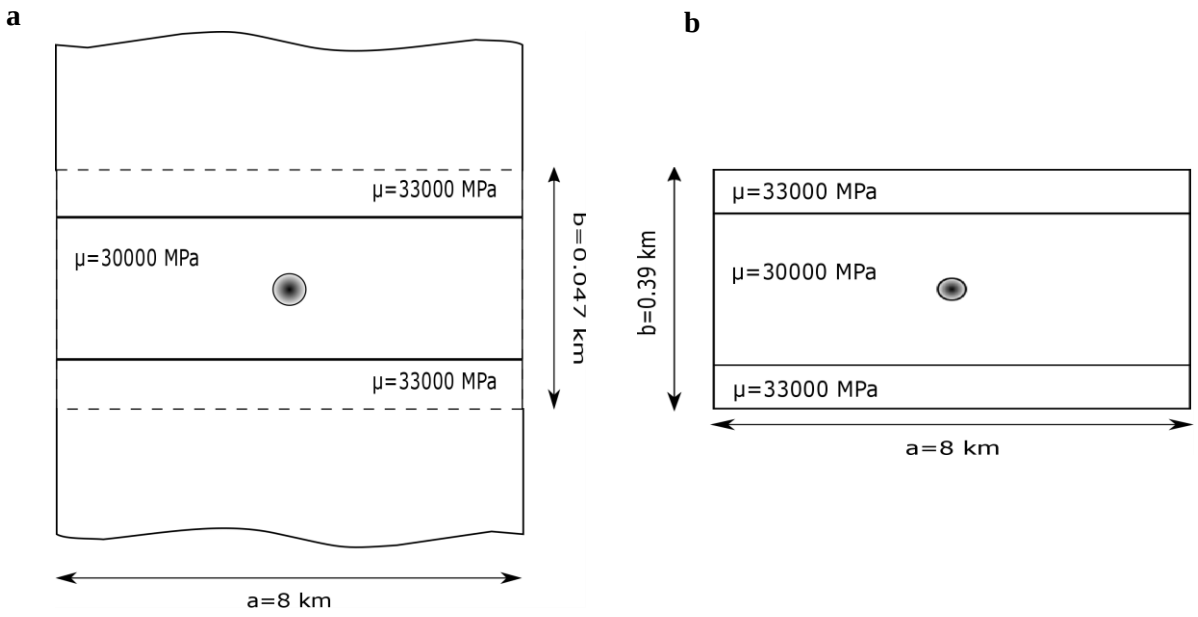

Figure 3.22- (a) Configuration of the problem in the Hybrid method. (b) Configuration of the problem in the FD method.

The rest of the model properties are the same as in the previous examples.

It is quite evident from the figures that follow, that even with heterogeneity, the two methods yield similar results and show very low levels of error. This is of high significance since it proves that with the hybrid method, we will be able to explore problems with heterogeneity by isolating the inhomogeneities in a virtual strip.

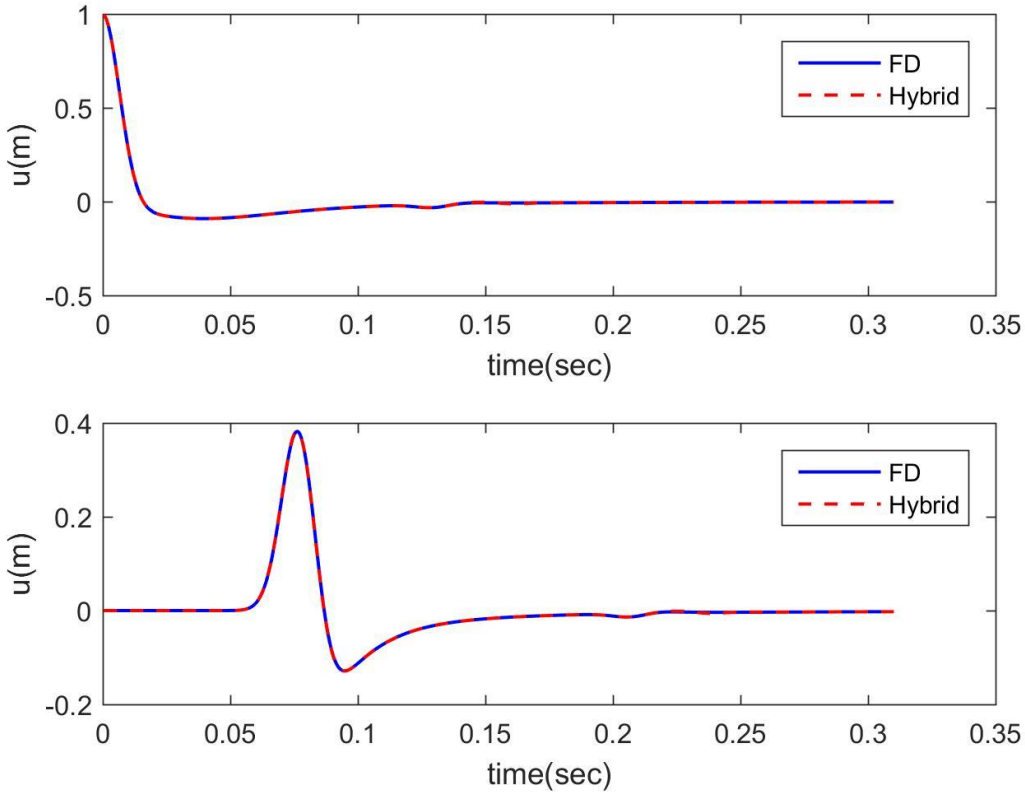

Figure 3.23- Time history plots. Top: Time history of a point at the middle of the strip. Bottom: Time history of a point at the center of the boundary.

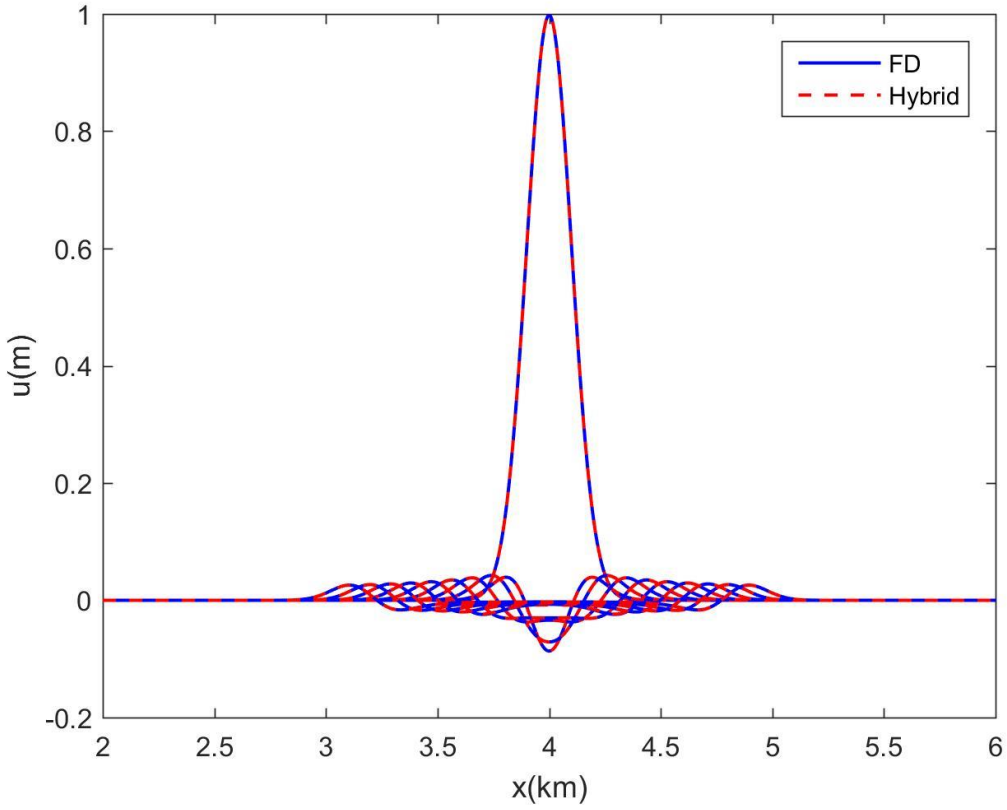

Figure 3.24- Comparison of the displacement profile along a line parallel to the x_1 axis and at the middle of the strip for the two methods. The displacement plots are provided every 100 time steps with time increasing as the maximum peak values decrease.

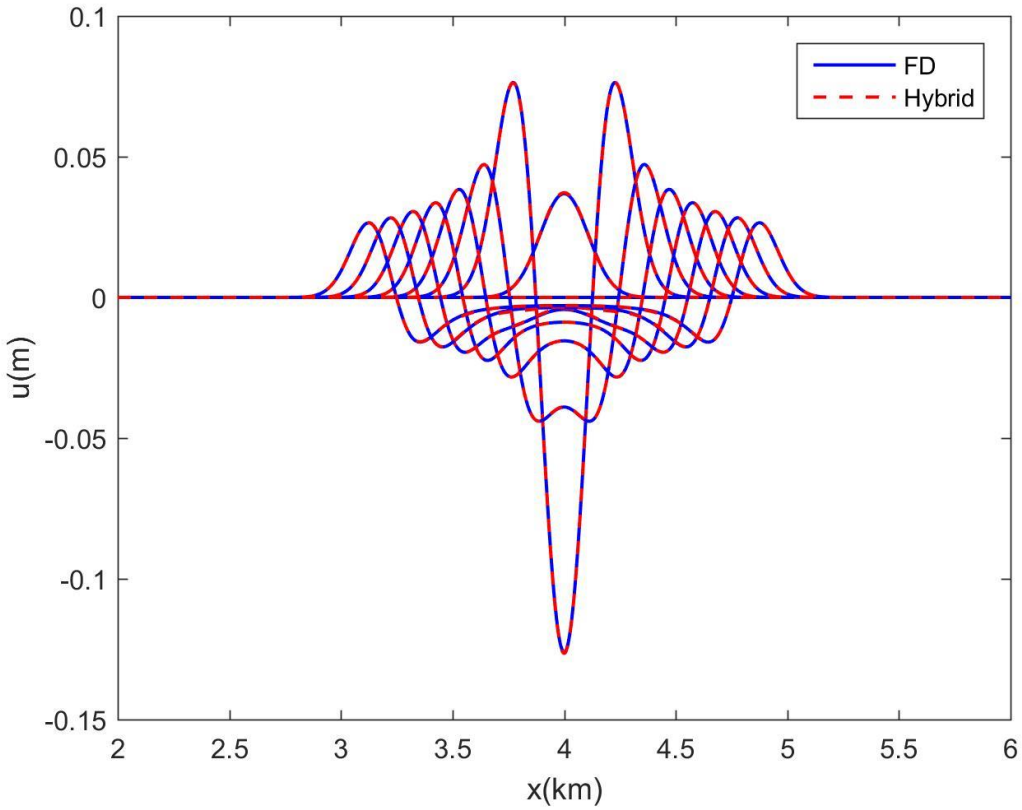

Figure 3.25- Comparison of the displacement profile along a line parallel to the x_1 axis and at the boundary of the strip for the two methods. The displacement plots are provided every 100 time steps with time increasing as the peaks move from the center to the sides.

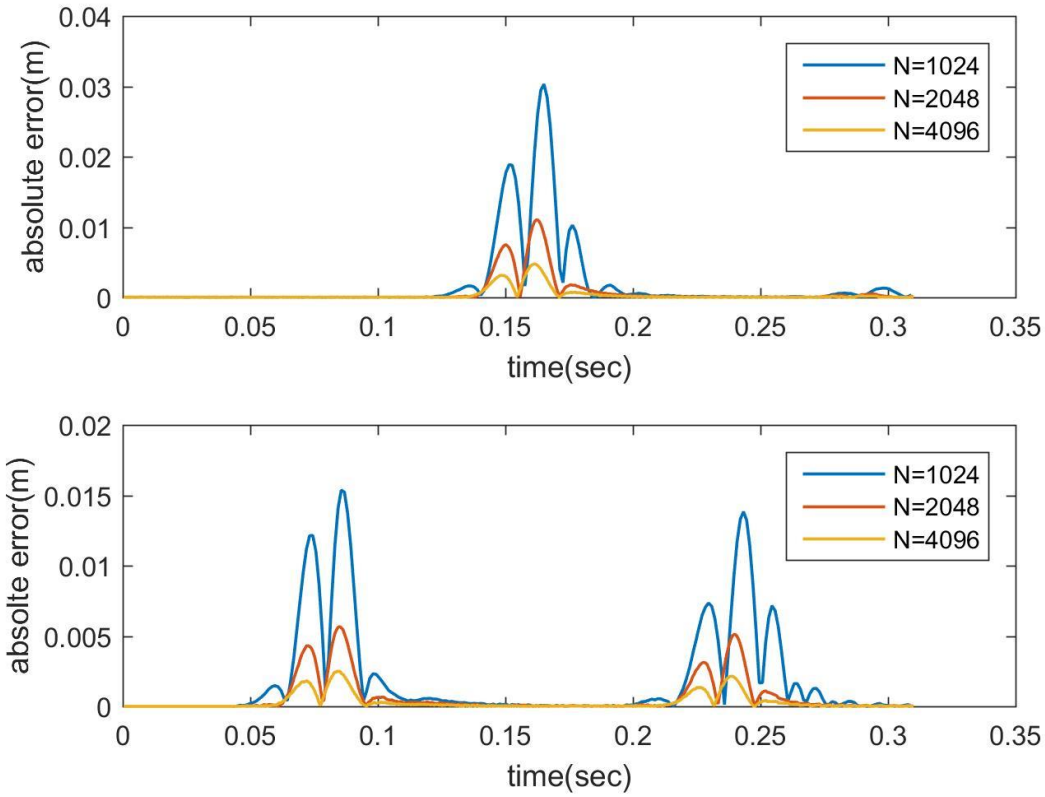

Figure 3.26- Error analysis plots. Top: error values for a point at the center of the strip. Bottom: error values for a point at the middle of the boundary.

3.5. Slip-weakening crack with low velocity fault zone

The configuration of the problem is similar to the one in section 3.3 except that the bulk is no longer entirely homogeneous. A slip-weakening law is considered along the crack and the same model properties as before are used.

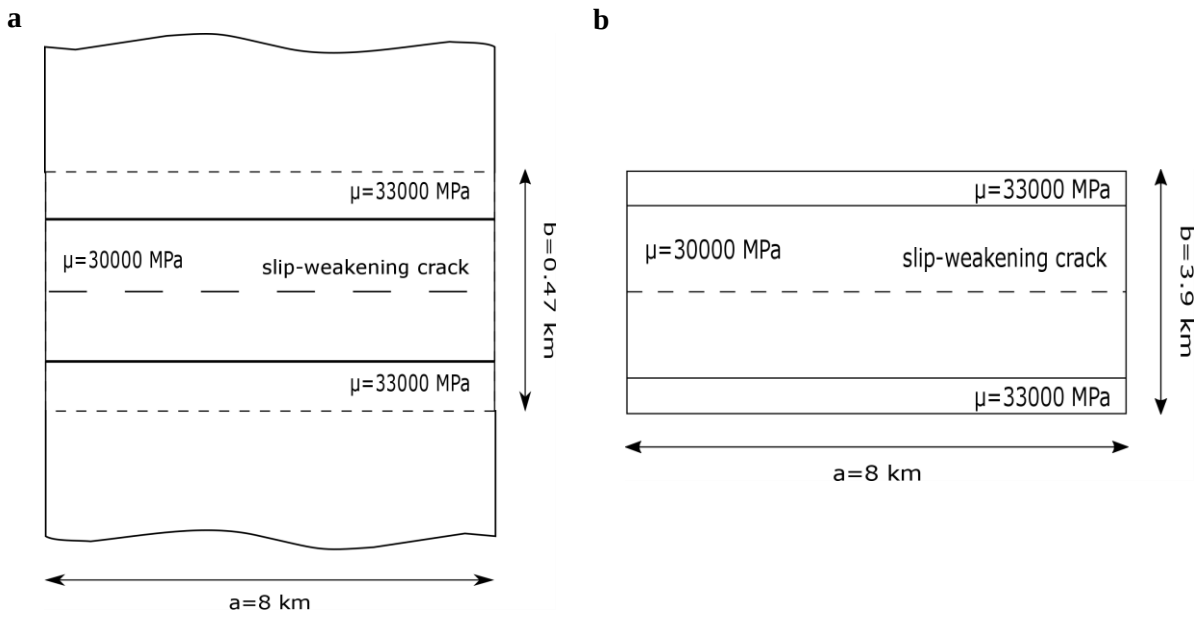

Figure 3.27- (a) Configuration of the problem in the Hybrid method. (b) Configuration of the problem in the FD method.

Figures 3.28 through 3.30 show the results for the most refined mesh. As it can be seen, the results match and show very low levels of error and the errors decrease with further mesh refinements.

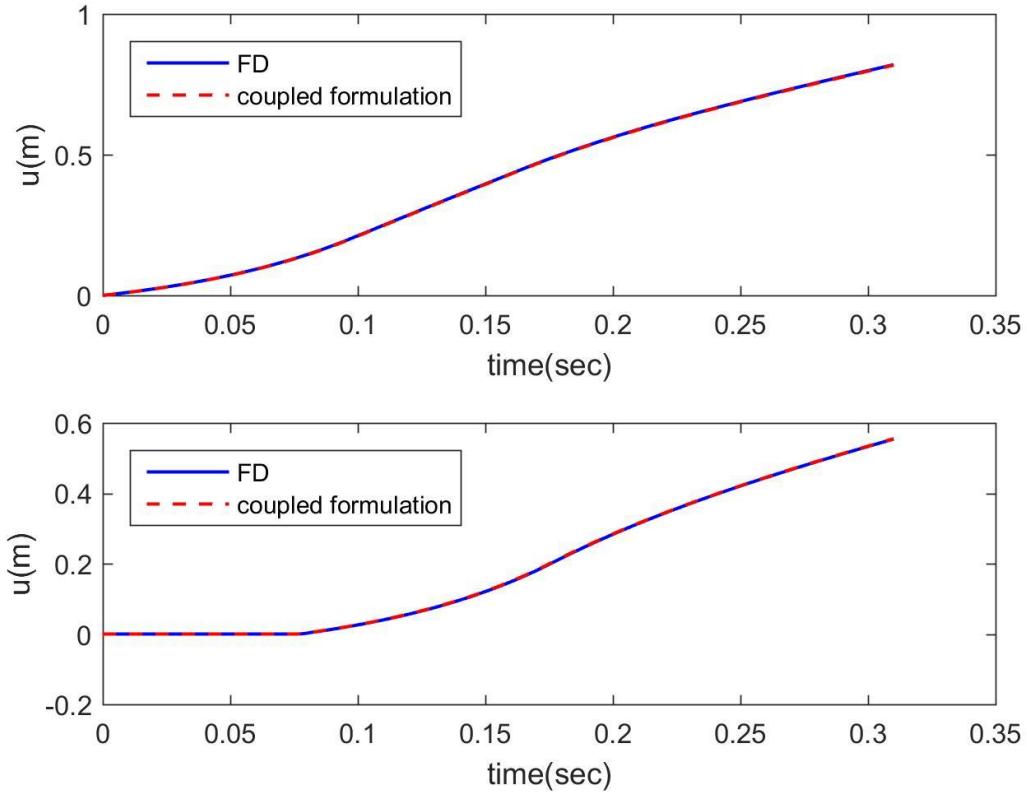

Figure 3.28- Time history plots. Top: Time history of a point at the middle of the crack on the upper halfplane. Bottom: Time history of a point at the center of the upper boundary of the strip.

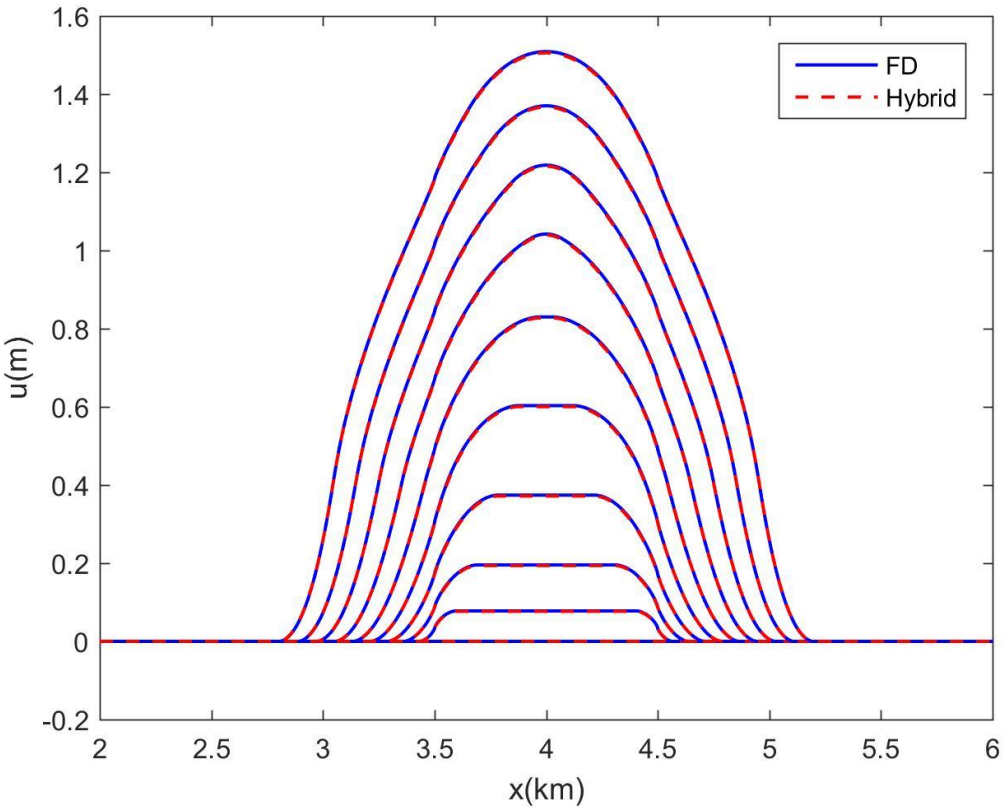

Figure 3.29- Comparison of the slip profiles along the crack for the two methods. The plots are provided every 100 time steps with time increasing as the maximum peak values increase.

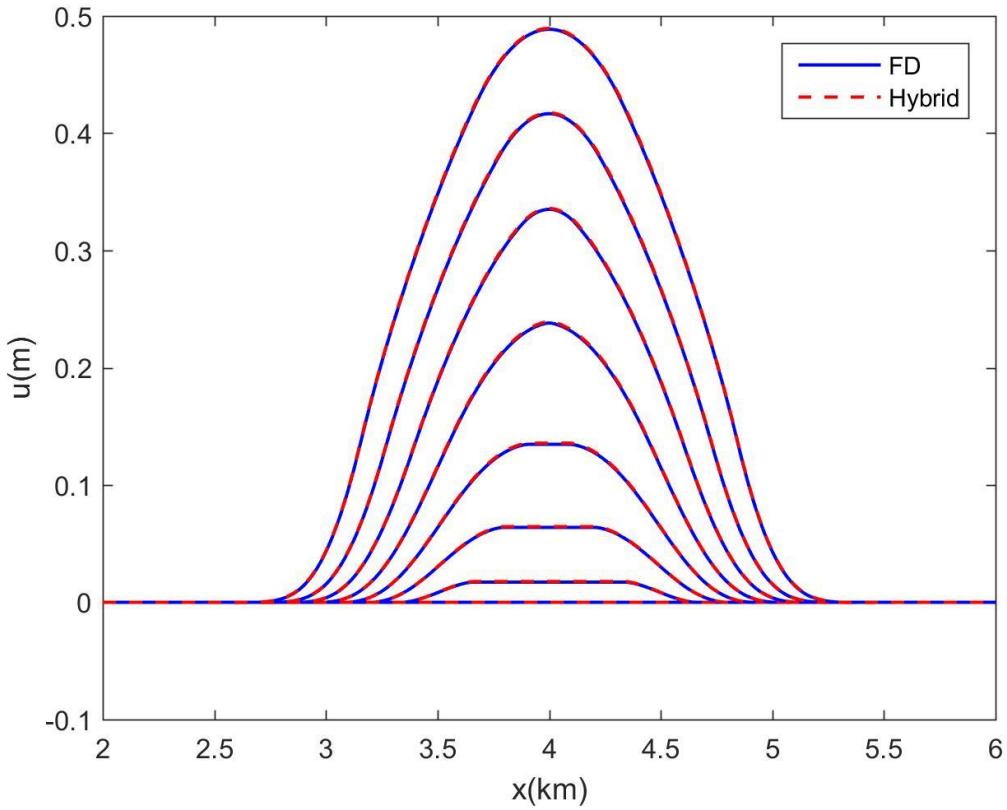

Figure 3.30- Comparison of the displacement profiles along a line parallel to the x_1 axis and on the upper boundary of the strip for the two methods. The displacement plots are provided every 100 time steps with time increasing as the peak values increase.

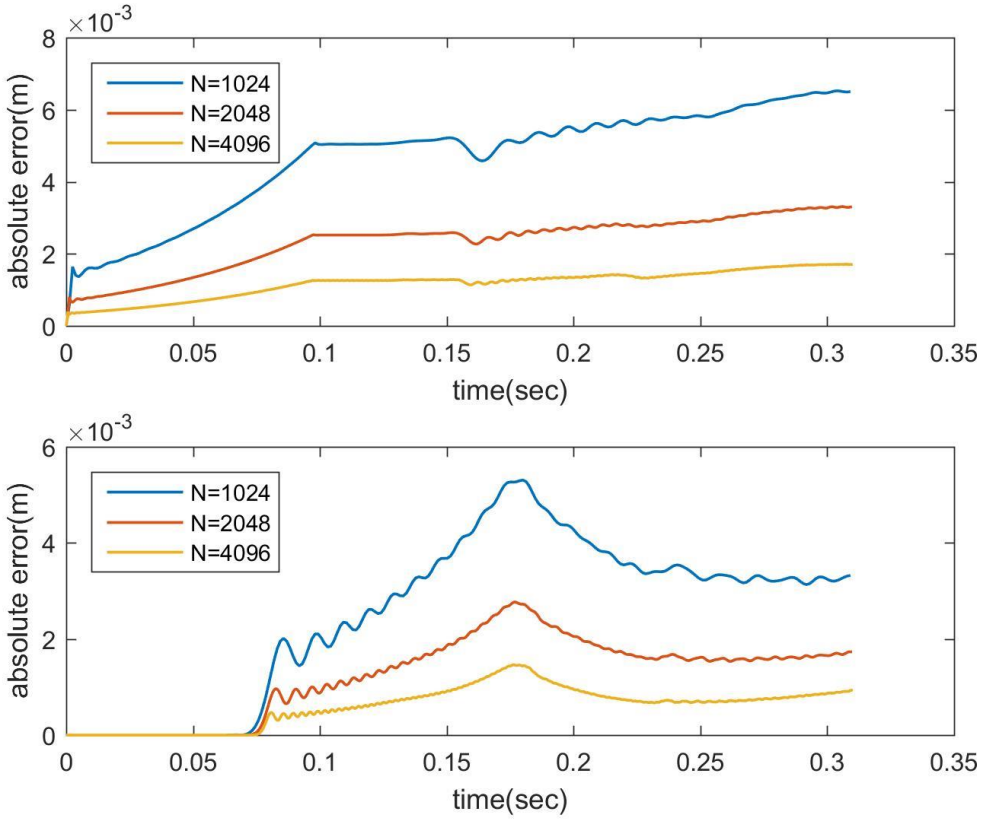

Figure 3.31- Error analysis plots. Top: absolute error of the slip values for a point at the center of the crack. Bottom: absolute error of the displacement values for a point at the middle of the boundary. It can be seen that the error is decreasing as the mesh becomes finer.

CHAPTER 4

CONCLUSIONS AND FUTURE WORK

Although there has been great progress in resolving the spatiotemporal complexities of earthquake ruptures, there's still a need to develop a numerical algorithm that is capable of long time simulation of earthquake cycles in a bulk that may have material heterogeneity, material nonlinearity or fault surface complexity. To that end, this work proposes a new hybrid numerical scheme in which the finite difference method and the boundary integral equation method are combined. This new method benefits from the flexibility of FD as well as the computational efficiency of BIEM and aims to enable treating fault zone nonlinearities and heterogeneities with unprecedented resolution.

The accuracy and credibility of this method can be assessed from the results presented in chapter 3 for the various problems studied. The first problem which examines a Gaussian source embedded in a linear elastic homogeneous medium serves as a simple example to put the Hybrid method to test by comparing the results with a pure FD scheme. It can be seen from figures 3.3 through 3.6 that the results match and the levels of error are low. The second example, aims to assess how the methods compare when the source has sharp discontinuities. A square source has been chosen for this purpose in the same setting as the previous example. It is concluded that the results are still compatible with the Hybrid method offering a somewhat smoother solution than the FD leading us to posit that the Hybrid method may be a better choice in comparison with FD when it comes to discontinuous wave sources. The levels of error are still low and they decrease with further mesh refinement. The third and fourth examples look at the problem of a spontaneously propagating shear crack embedded in a linear elastic homogeneous medium. One studies a shear crack with constant friction and the other uses the more realistic assumption of a

slip-weakening friction law. The results of both examples confirm the accuracy and convergence of the Hybrid method. The last two examples, which are of more significance, implement the idea of isolating heterogeneities—both in the presence and absence of a discontinuity surface—in a virtual strip and coupling this strip with two half-spaces through modeling their elastodynamic response by the independent spectral boundary method. It is established from the results presented in chapter 3 for these two cases that the hybrid and the pure FD methods yield very similar results and the levels of error in the hybrid approach are low. Furthermore, mesh refinement proves beneficial in reducing errors which guarantees convergence.

From what has been explained above, it can be concluded that the Hybrid method has proved to be successful in modeling various problems—from volumetric sources in linear elastic media to cracks embedded in a continuum with heterogeneities. This is very promising since it provides us with a tool for exploring new problems such as modeling faults with plasticity or multiple cracks.

This method can also provide us with the means of looking into problems with nonplanar fault segments, which have not been rigorously studied except for a few recent solutions proposed in the works of *Cruz-Atienza and Virieux*, 2004, *Kase and Day*, 2006, *Zhang et al.*, 2004; *Dunham et al.,* 2011. The Hybrid method can also be a harbinger for coupling the boundary integral method with the Finite Element method instead of FD in an attempt to improve numerical performance.

Last but not least, one of the most important problems to look into will definitely be cycle simulations of earthquakes in a bulk containing material heterogeneity, material nonlinearity or fault surface complexity. We believe that the hybrid method provides us with an unprecedented

tool to address this problem for two primary reasons. First, the independent spectral boundary integral formulation enables accurate near field truncation of the wave field eradicating the need for discretizing a significant portion of the bulk and thus leading to significant computational saving. Furthermore, compared to other known absorbing boundary conditions or layers, the integral formulation is accurate in both dynamic and quasidynamic limits and thus will be capable of handling both the dynamics and interseismic portions of the seismic cycle. Second, adopting the spectral formulation will enable us to leverage the infrastructure developed by Lapusta et al. (2000) regarding mode truncation and adaptive time stepping, after being properly adapted to the hybrid approach, allowing efficient simulation of the seismic history.

APPENDIX A

We attempt to solve the following boundary value problem on a strip of width *a* and thickness *b*.

$$\begin{cases} u_{tt} = c_s^2 \left(u_{xx} + u_{yy}\right) \\ u(0,y,t) = u(a,0,t) = 0 \\ u(x,0,t) = u(x,b,t) = 0 \\ u(x,y,0) = f(x,y) \\ u_t(x,y,0) = 0 \end{cases} \tag{A.1}$$

where $c_s = \sqrt{\frac{\mu}{\rho}}$ is the shear wave speed and $f(x,y)$ represents the volumetric source.

In seismology, a finite volume of the earth is usually extracted for studying. Therefore, we choose the dimensions of the strip large enough so as to avoid having any artificial reflections from the model boundaries during the simulation period (Aochi et al., 2013).

Discretization of the 2-D equation

A rectangular grid is introduced to discretize the strip as it can be seen in Fig.(A.1).[2]

$$x_i = i\,\Delta x \qquad i = 0, \dots, N_{ele_x} \tag{A.2}$$

$$y_j = j\,\Delta y \qquad j = 0, \dots, N_{ele_y} \tag{A.3}$$

Time is also discretized such that

$$t_k = k\,\Delta t \qquad k = 0, \dots, N_{ele_t} \tag{A.4}$$

Here, N_{ele_x} and N_{ele_y} represent the number of elements in the *x* and *y* directions respectively and $Nele_t$ shows the number of time steps.

[2] The node numbering starts from the left-most node at the bottom, which coincides with the origin of the coordinate system.

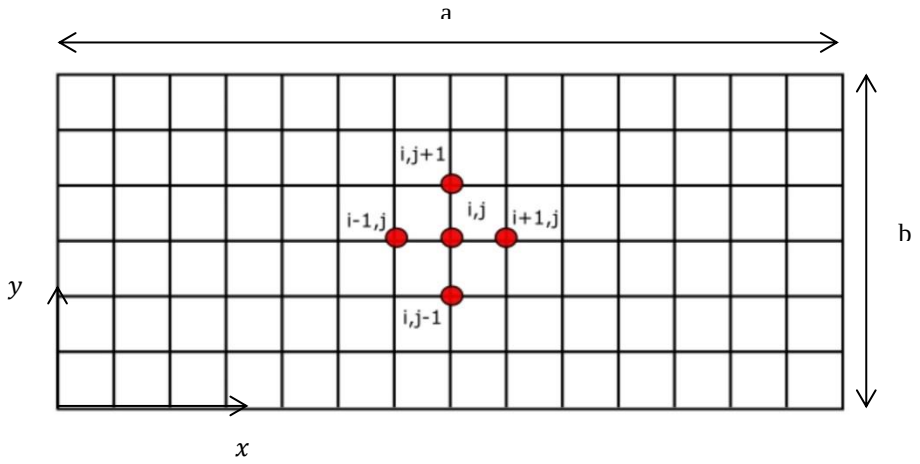

Fig. (A.1)- 2-D discretization of the strip.

The approximate derivatives using 2nd order central differences are as follow

$$u_{tt}(x_i, y_j, t_k) \approx \frac{u_{i,j}^{k+1} - 2u_{i,j}^{k} + u_{i,j}^{k-1}}{\Delta t^2} \tag{A.5}$$

$$u_{xx}(x_i, y_j, t_k) \approx \frac{u_{i+1,j}^{k} - 2u_{i,j}^{k} + u_{i-1,j}^{k}}{\Delta x^2} \tag{A.6}$$

$$u_{yy}(x_i, y_j, t_k) \approx \frac{u_{i,j+1}^{k} - 2u_{i,j}^{k} + u_{i,j-1}^{k}}{\Delta y^2} \tag{A.7}$$

Defining $r = c_s \frac{\Delta t}{\Delta x}$ and plugging the above equations into (A.1) yields the following discretized formulation for the problem

$$u_{i,j}^{k+1} = 2\,u_{i,j}^{k} - u_{i,j}^{k-1} + r^2\left(u_{i+1,j}^{k} + u_{i-1,j}^{k} + u_{i,j+1}^{k} + u_{i,j-1}^{k} - 4\,u_{i,j}^{k}\right) \tag{A.8}$$

where *i* and *j* represent node numbers in the *x* and *y* directions, respectively and *k* shows discretization in time.

Initial conditions

There are two initial conditions that can be written as follows in discrete form. The initial conditions on velocity will help us determine the displacement values at the ghost points.

$$u(x,y,0) = f(x,y) \;\rightarrow\; u_{i,j}^{0} = f\left(x_i, y_j\right) \qquad i = 0,\dots,N_{ele_x} \qquad j = 0,\dots,N_{ele_y} \tag{A.9}$$

$$\begin{aligned} u_t(x,y,0) = 0 \qquad &\rightarrow \qquad \frac{u_{i,j}^{0} - u_{i,j}^{-1}}{\Delta t} = 0 \\ &\rightarrow\; u_{i,j}^{-1} = u_{i,j}^{0} \qquad i = 0,\dots,N_{ele_x} \quad j = 0,\dots,N_{ele_y} \end{aligned} \tag{A.10}$$

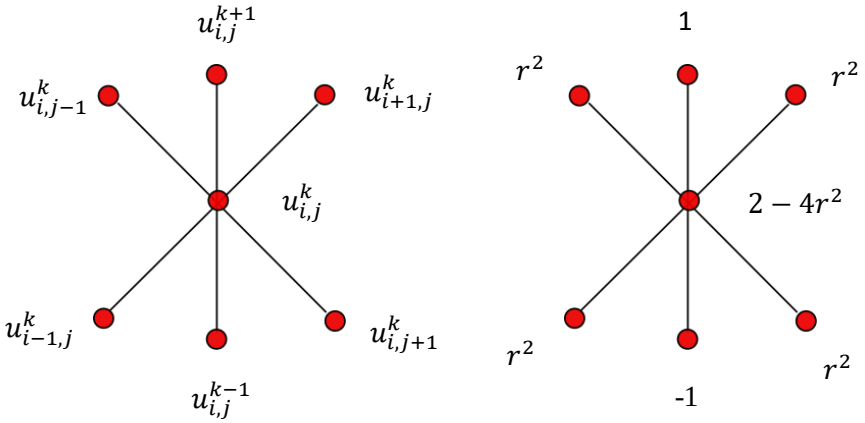

Fig. (A.2)- Computational molecule (stencil) in (x, y, t) space.

The $u_{i,j}^{-1}$ ghost points are determined in this manner.

Boundary conditions

As it can be seen from Equation (A.1), the displacement values are set to zero on the boundaries, but the plate dimensions are chosen large enough to avoid reflections from the fixed boundaries.

Updating scheme

1. Define variables $u_{i,j}^{+}, u_{i,j}, u_{i,j}^{-}$ for $u_{i,j}^{k+1}, u_{i,j}^{k}, u_{i,j}^{k-1}$
2. Set $t = 0$ and $r = c_s \frac{\Delta t}{\Delta x}$
3. Set initial conditions

$$u_{i,j} = f(x_i, y_j) \qquad i = 0, \dots, N_{ele_x} \qquad j = 0, \dots, N_{ele_y} \tag{A.11}$$

4. Set $u_{i,j}^{-} = u_{i,j}$

5. While $t < t_{stop}$

- $t = t + \Delta t$
- Update all inner points by Equation (A.8) obtained in the previous section:

$$u_{i,j}^{+} = 2\,u_{i,j} - u_{i,j}^{-} + r^2\left(u_{i+1,j} + u_{i-1,j} + u_{i,j+1} + u_{i,j-1} - 4u_{i,j}\right) \tag{A.12}$$

- Set the boundary conditions:

$$\begin{aligned} u_{0,j}^{+} &= 0 \qquad j = 0, \dots, N_{ele_y} \\ u_{N_{ele_x},j}^{+} &= 0 \qquad j = 0, \dots, N_{ele_y} \\ u_{i,0}^{+} &= 0 \qquad i = 0, \dots, N_{ele_x} \\ u_{i,N_{ele_y}}^{+} &= 0 \qquad i = 0, \dots, N_{ele_x} \end{aligned} \tag{A.13}$$

- Update variables for next round:

$$u_{i,j}^{-} = u_{i,j}\,; \quad u_{i,j} = u_{i,j}^{+} \tag{A.14}$$

APPENDIX B

The spectral representation is based on a Fourier representation, in spatial coordinates along a fracture plane in an infinite homogeneous, linearly elastic body, of the tractions and relative displacements (opening and shear). The formulation embodies an exact elastodynamic representation of the relation existing between the Fourier coefficients for the tractions and corresponding displacement discontinuities (Geubelle & Rice, 1995). There are two versions of spectral algorithms: in the first approach, referred to as the *independent spectral formulation*, the elastodynamic response of each halfspace is studied separately and then the two halfspaces are connected by imposing appropriate boundary conditions on the interface. In the second approach, referred to as the *combined spectral formulation* as suggested by *Breitenfeld and Geubelle* [1998], the formulation of the problem is written in a way to combine the elastodynamic analysis of the two halfspaces into one. The two approaches are based on the same principles and often yield similar results. However, they do have minor differences in their formulation and implementation and show different stability characteristics when it comes to in-plane modes (Breitenfeld & Geubelle, 1998). Here, we proceed to explain the derivation of the independent spectral formulation, which was first introduced for three-dimensional fracture problems by *Geubelle and Rice* [1995], for a simpler 2-D antiplane case.

Define the Cartesian coordinates such that the fracture plane coincides with $x_2 = 0$. Therefore, x_1 and x_3 are coordinates in the plane of the crack and elastodynamic fields will exist in the two halfspaces $x_2 > 0$ and $x_2 < 0$.

Consider the propagation of an antiplane 2-D shear crack in x_3 direction. The only nonzero component of displacement, in this case, is u_3 and we have

$$c_s^2\, u_{3,\alpha\alpha} = u_{3,tt} \qquad \alpha = 1,2 \tag{B.1}$$

$$c_s^2\, \Delta u_3 = u_{3,tt} \tag{B.2}$$

Let's examine one particular spectral component,

$$u_3(x_\alpha, t) = e^{iqx_1}\, \Omega(x_2, t; q) \tag{B.3}$$

The Laplace transform in the time domain is

$$\hat{f}(p) = L[f(t)] = \int_0^\infty e^{-pt} f(t) dt \tag{B.4}$$

Rewriting Equation (B.2), we get

$$c_s^2 \left(\frac{\partial^2 u_3}{\partial x_1^2} + \frac{\partial^2 u_3}{\partial x_2^2} \right) = u_{3,tt} \tag{B.5}$$

Applying the Fourier transform,

$$c_s^2 \left(-q^2 \Omega + \frac{\partial^2 \Omega}{\partial x_2^2} \right) = \Omega_{tt} \tag{B.6}$$

Applying the Laplace transform,

$$c_s^2 \left(-q^2 \widehat{\Omega} + \frac{\partial^2 \widehat{\Omega}}{\partial x_2^2} \right) = p^2 \widehat{\Omega} \tag{B.7}$$

Define $\widehat{\Omega}'' = \frac{\partial^2 \widehat{\Omega}}{\partial x_2^2}$. Equation (7) can be rewritten as a second order ODE.

$$\widehat{\Omega}''(x_2, p; q) = q^2 \left(1 + \frac{p^2}{q^2 c_s^2} \right) \widehat{\Omega}(x_2, p; q) \tag{B.8}$$

Introduce,

$$\alpha_s = \sqrt{1 + \frac{p^2}{q^2 c_s^2}} \tag{B.9}$$

Equation (B.8) can be rewritten as,

$$\widehat{\Omega}''(x_2, p; q) = q^2 \alpha_s^2 \, \widehat{\Omega}(x_2, p; q) \tag{B.10}$$

The PDE is now reduced to a 2nd order ODE that we can solve.

$$characteristic\ equation: \qquad r^2 - q^2\alpha_s^2 = 0 \qquad \rightarrow \qquad r = \mp |q| \alpha_s \tag{B.11}$$

Considering the radiation condition for the upper half-space and ignoring the unbounded solution, we will get

$$\widehat{\Omega}(x_2, p; q) = \widehat{\Omega}_0(p; q) e^{-|q|\alpha_s x_2} \tag{B.12}$$

where $\widehat{\Omega}_0(p; q) = \widehat{\Omega}(0, p; q)$.

We are only concerned with the tractions along the fracture plane $x_2 = 0$ and the resulting displacements. Therefore, define the Fourier coefficients by

$$u_3^+ \, (x_1, x_2 = 0^+; t) = U_3^+(t; q) e^{iqx_1} \tag{B.13}$$

Use Equations (B.3) and (B.12) to get

$$\begin{aligned} \hat{u}_3(x_\alpha, p) &= e^{iqx_1} \widehat{\Omega}_0 e^{-|q|\alpha_s x_2}, \\ \hat{u}_3(x_1, x_2 = 0^+; t) &= \widehat{\Omega}_0 e^{iqx_1}, \\ \hat{u}_3(x_\alpha, p) &= e^{iqx_1} \widehat{U}_3^+(p; q) e^{-|q|\alpha_s x_2} \end{aligned} \tag{B.14}$$

Writing $\tau_j(x_1, t)$ for the traction component of stress along the fracture plane

$$\tau_3^+(x_1, t) = \sigma_{23}^+(x_1, x_2 = 0^+, t) = T_3^+(t; q) e^{iqx_1} \tag{B.15}$$

We know,

$$\sigma_{ij} = \lambda\delta_{ij}u_{k,k} + \mu\left(u_{i,j} + u_{j,i}\right) \tag{B.16}$$

where λ and μ are Lamé constants.

$$\begin{aligned}
\sigma_{23} &= \mu\left(u_{2,3} + u_{3,2}\right) = \mu\, u_{3,2} \\
\hat{\sigma}_{23} &= \mu\,(\hat{u}_3)_{,2} = -\mu|q|\alpha_s e^{iqx_1}\widehat{U}_3(p;q)e^{-|q|\alpha_s x_2}, \\
\hat{\tau}_3^+(x_1,t) &= \hat{\sigma}_{23}^+(x_1, x_2 = 0^+, t) = T_3^+(p;q)e^{iqx_1},
\end{aligned} \tag{B.17}$$

And,

$$\hat{\sigma}_{23}^+(x_1, x_2 = 0^+, t) = -\mu|q|\alpha_s\widehat{U}_3(p;q)e^{iqx_1} \tag{B.18}$$

Therefore,

$$T_3^+(p;q) = -\mu|q|\alpha_s\widehat{U}_3(p;q) \tag{B.19}$$

The right-hand side of this equation can be rewritten by explicitly extracting the instantaneous response $-\frac{\mu\, p}{c_s}\widehat{U}_3(p;q)$.

Hence,

$$T_3^+(p;q) = -\frac{\mu\, p}{c_s}\widehat{U}_3(p;q) - \mu|q|\left(\alpha_s - \frac{p}{|q|c_s}\right)\widehat{U}_3(p;q) \tag{B.20}$$

Back in the time domain, we have

$$\tau_3^+(x_1,t) = \tau_3^{0^+}(x_1,t) - \frac{\mu}{c_s}\dot{u}_3^+(x_1,t) + f_3^+(x_1,t) \qquad upper\ halfspace \tag{B.21}$$

Following a similar procedure for the lower halfspace and imposing the radiation condition for $x_2 < 0$, will similarly lead to

$$\tau_3^-(x_1,t) = \tau_3^{0^-}(x_1,t) + \frac{\mu}{c_s}\dot{u}_3^-(x_1,t) + f_3^-(x_1,t) \qquad lower\ halfspace \tag{B.22}$$

REFERENCES

Andrews, D. J. (1976). Rupture propagation with finite stress in antiplane strain. *Journal of Geophysical Research, 81*(20), 3575-3582. doi:10.1029/JB081i020p03575

Aochi, H., Ulrich, T., Ducellier, A., Dupros, F., & Michea, D. (2013). *Finite Difference Simulations of Seismic wave Propagation for Understanding Earthquake Physics and Predicting Ground Motions: Advances and Challenges.* Paper presented at the 24th IUPAP Conference on Computational Physics (IUPAP-CCP 2012), 14-18 Oct. 2012, UK.

Archuleta, R. J., & Day, S. M. (1980). Dynamic rupture in a layered medium: the 1966 Parkfield earthquake. *Bulletin of the Seismological Society of America, 70*(3), 671-689.

Berenger, J. P. (1994). A perfectly matched layer for the absorption of electromagnetic waves. *Journal of Computational Physics, 114*(2), 185-200. doi:10.1006/jcph.1994.1159

Bettess, P. (1977). Infinite elements. *International Journal for Numerical Methods in Engineering, 11*(1), 53-64. doi:10.1002/nme.1620110107

Boore, D. M., Larner, K. L., & Aki, K. (1971). Comparison of two independent methods for the solution of wave- scattering problems: Response of a sedimentary basin to vertically incident SH waves. *Journal of Geophysical Research, 76*(2), 558-569. doi:10.1029/JB076i002p00558

Breitenfeld, M. S., & Geubelle, P. H. (1999). Numerical analysis of dynamic debonding under 2D in-plane and 3D loading. *International Journal of Fracture, 93*(1), 13-38.

Cochard, A., & Madariaga, R. (1994). Dynamic faulting under rate-dependence friction. *Pure and Applied Geophysics, 142*(3-4), 419-445. doi:10.1007/BF00876049

Cruz-Atienza, V. M., & Virieux, J. (2004). Dynamic rupture simulation of non-planar faults with a finite-difference approach. *Geophysical Journal International, 158*(3), 939-954. doi:10.1111/j.1365-246X.2004.02291.x

Das, S., & Aki, K. (1977). A numerical study of two-dimensional spontaneous rupture propagation. *Geophysical Journal of the Royal Astronomical Society, 50*(3), 643-668.

Day, S. M. (1982). Three-dimensional finite difference simulation of fault dynamics: rectangular faults with fixed rupture velocity. *Bulletin of the Seismological Society of America, 72*(3), 705-727.

Day, S. M., Dalguer, L. A., Lapusta, N., & Liu, Y. (2005). Comparison of finite difference and boundary integral solutions to three-dimensional spontaneous rupture. *Journal of Geophysical Research, 110*(B12). doi:10.1029/2005jb003813

Dunham, E. M., Belanger, D., Cong, L., & Kozdon, J. E. (2011). Earthquake ruptures with strongly rate-weakening friction and off-fault plasticity, part 2: Nonplanar faults. Bulletin of the Seismological Society of America, 101(5), 2308-2322. doi:10.1785/0120100076

Geubelle, P. H., & Rice, J. R. (1995). A spectral method for three-dimensional elastodynamic fracture problems. *Journal of the Mechanics and Physics of Solids, 43*(11), 1791-1824. doi:10.1016/0022-5096(95)00043-I

Ida, Y. (1972). Cohesive force across the tip of a longitudinal-shear crack and Griffith's specific surface energy. *Journal of Geophysical Research, 77*(20), 3796-3805. doi:10.1029/JB077i020p03796

Kase, Y., & Day, S. M. (2006). Spontaneous rupture processes on a bending fault. *Geophysical Research Letters, 33*(10). doi:10.1029/2006GL025870

Kaser, M., & Dumbser, M. (2006). An arbitrary high-order discontinuous Galerkin method for elastic waves on unstructured meshes. I. The two-dimensional isotropic case with external source terms. *Geophysical Journal International, 166*(2), 855-877. doi:10.1111/j.1365-246X.2006.03051.x

Komatitsch, D., & Tromp, J. (1999). Introduction to the spectral element method for three-dimensional seismic wave propagation. *Geophysical Journal International, 139*(3), 806-822. doi:10.1046/j.1365-246x.1999.00967.x

Kozdon, J. E., Dunham, E. M., & Nordstrom, J. (2013). Simulation of Dynamic Earthquake Ruptures in Complex Geometries Using High-Order Finite Difference Methods. *Journal of Scientific Computing, 55*(1), 92-124. doi:10.1007/s10915-012-9624-5

Lapusta, N., Rice, J. R., Ben-Zion, Y., & Gutuan, Z. (2000). Elastodynamic analysis for slow tectonic loading with spontaneous rupture episodes on faults with rate- and state-dependent friction. *Journal of Geophysical Research, 105*(B10), 23765-23789. doi:10.1029/2000JB900250

Lysmer, J. and R.L. Kuhlemeyer, “Finite dynamic model for infinite media”, Journal of the Engineering Mechanics Division, Proc. ASCE, vol. 95, no. EM4, 1969.

Madariaga, R., Olsen, K., & Archuleta, R. (1998). Modeling dynamic rupture in a 3D earthquake fault model. *Bulletin of the Seismological Society of America, 88*(5), 1182-1197.

Palmer, A. C., & Rice, J. R. (1973). GROWTH OF SLIP SURFACES IN PROGRESSIVE FAILURE OF OVER-CONSOLIDATED CLAY. *Proceedings of the Royal Society of London Series a-Mathematical Physical and Engineering Sciences, 332*(1591), 527-548. doi:10.1098/rspa.1973.0040

Phuong, T., Kandula, S. S. V., Geubelle, P. H., & Sottos, N. R. (2008). Hybrid spectral/finite element analysis of dynamic delamination of patterned thin films. *Engineering Fracture Mechanics, 75*(14), 4217-4233. doi:10.1016/j.engfracmech.2008.03.006

Virieux, J., & Madariaga, R. (1982). Dynamic faulting studied by a finite difference method. *Bulletin of the Seismological Society of America, 72*(2), 345-369.

Zhang, W., Iwata, T., Irikura, K., Pitarka, A., & Sekiguchi, H. (2004). Dynamic rupture process of the 1999 Chi-Chi, Taiwan, earthquake. *Geophysical Research Letters, 31*(10), 4 pp. doi:10.1029/2004GL019827